Stimulus-induced theta band LFP oscillations format spiking outputs in the mouse accessory olfactory bulb

Oksana Cohen[*1], Anat Kahan[*1], Idan Steinberg[1], Sebastian Malinowski[2], Dan Rokni[1], Marc Spehr[2], Yoram Ben-Shaul[1+]

1. Department of Medical Neurobiology, Institute for Medical Research Israel Canada, Faculty of Medicine, The Hebrew University of Jerusalem, Jerusalem, Israel
2. Department of Chemosensation, Institute for Biology II, RWTH Aachen University, Aachen, Germany.
+ Corresponding author
* These authors contributed equally

Key Points

- Prominent theta band LFP oscillations, distinct from breathing-induced main olfactory bulb oscillations, are present in the accessory olfactory bulb
- The oscillations represent the peak of an ongoing network state that depends on sensory stimulation
- The LFP signature reflects stimulus features
- LFP oscillations are most prominent in the external cell layer and likely involve an interaction between AOB mitral cells and granule cells
- Action potentials of individual AOB neurons favor the negative phase of LFP oscillations
- The oscillations could bind and potentially multiplex outputs from individual AOB neurons to downstream processing stages

Abstract

The vomeronasal system (VNS) is dedicated to processing ethologically relevant chemosensory cues from other organisms. Its first central processing stage is the accessory olfactory bulb (AOB), which sends information to downstream brain regions via spiking activity of its principal neurons, AOB mitral cells (AOB-MCs). Recent studies provided important insights about the functional properties of AOB-MCs and the stimulus aspects that they encode. However, very little is known about the principles that govern their coordinated activity and the manner by which AOB outputs are relayed to downstream regions. In many brain regions, network oscillations play a key role in orchestrating the activity of output neurons, and thereby facilitate and enhance transmission of information. A widely used readout of network processes and oscillations is the local field potential (LFP), which has been extensively studied in the main olfactory system (MOS) and, specifically, in the main olfactory bulb (MOB). To reveal population-level processes in the AOB, we analyzed LFP signals while presenting natural stimuli to anesthetized adult male and female mice. Our recordings reveal prominent LFP theta band oscillatory episodes with a characteristic spatial pattern across the AOB. Using a template matching approach, we find that network dynamics show varying degrees of similarity to this pattern throughout an experiment. Notably, both the similarity to this pattern, and the intensity of the pattern, are modulated by stimulus features. Analysis of LFP signal polarity and its spatial relationship to single unit activity, indicate that oscillatory episodes are generated locally within the AOB, likely representing a reciprocal interaction between AOB-MCs and granule cells (GCs). Co-examination of single unit and LFP activity suggests that oscillations appear when sensory activation surpasses a certain threshold. Importantly, spike times of many AOB-MCs are constrained to the negative LFP oscillation phase, in a manner that can drastically effect integration by downstream processing stages.

Based on these observations, we propose that these LFP oscillations can gate, bind, and potentially also multiplex outgoing signals from individual AOB neurons to downstream processing stages.

Introduction

Social, reproductive, and defensive behaviors are crucial for survival, and in many organisms their implementation depends on chemical signaling and processing. In most vertebrates, including mice, this function is served by the vomeronasal system (VNS), a compact but essential sensory system that is dedicated to processing chemical signals from other organisms (Mohrhardt et al., 2018, Dulac and Wagner, 2006, Dhawale et al., 2010). The VNS is often compared to, and in some ways resembles, the MOS. However, there are fundamental differences in their physiology and functional organization. A large body of studies revealed many aspects of VNS physiology. In particular, studies in both behaving (Luo et al., 2003) and anesthetized (Ben Shaul et al., 2010, Hendrickson et al., 2008) animals, and in *ex vivo* preparations (Meeks et al., 2010) examined spiking responses of neurons in the mouse AOB during sensory stimulation. These studies have shown that AOB neurons display low baseline rates, and typically respond to chemical stimuli from multiple sources (conspecifics and non-conspecifics) with rate elevations (Kahan and Ben-Shaul, 2016, Tolokh et al., 2013). Anatomically, the first brain relay of the VNS, the AOB, appears like an integrative network, in which its output neurons, AOB-MCs, sample activity from multiple input channels (Larriva-Sahd, 2008, Mohrhardt et al., 2018, Wagner et al., 2006). While individual vomeronasal ligands can elicit physiological and behavioral responses (Ishii and Touhara, 2019, Ishii et al., 2017, Kimoto et al., 2005, Li and Liberles, 2015, Ferrero et al., 2013), most natural vomeronasal stimuli are complex bodily secretions, which contain numerous chemical components. Correspondingly, information about complex stimulus blends is likely represented by AOB-MCs in a distributed manner (Kahan and Ben-Shaul, 2016, Ben-Shaul et al., 2010, Hammen et al., 2014, Fu et al., 2015, Tolokh et al., 2013).

In the MOS, it is well accepted that information about odorants is conveyed to downstream regions by the concerted activity of ensembles of output neurons (Buck, 2004, Malnic et al., 1999, Koulakov et al., 2007, Chong and Rinberg, 2018, Uchida et al., 2014). Extensive studies have revealed multiple processes that play a role in organizing and formatting output patterns of MOB neurons. Such processes are usually revealed by LFP signals, which typically reflect population-level activity (Einevoll et al., 2013, Buzsaki et al., 2012, Buzsáki, 2006). Specifically, a variety of olfactory bulb LFP oscillatory patterns, spanning the theta, beta, and gamma frequency ranges were described (Kay, 2015, Kay, 2014). Although the precise mechanisms underlying these oscillations are still under investigation (Li and Cleland, 2017, Kersen et al., 2022, Burton and Urban, 2021, Fourcaud-Trocme et al., 2018, Bathellier et al., 2006, Fukunaga et al., 2014), it is well established that they arise from both local (e.g., within the MOB) and global interactions (e.g., involving multiple olfactory brain regions), and are directly influenced by breathing, the fundamental action that determines MOS stimulus sampling. Together, these oscillatory patterns reflect processes that may gate, bind, and multiplex information, as it is transmitted from the olfactory bulb to downstream regions. More specifically, activity of neurons with respect to each other, or with respect to the breathing cycle, can be informative about the stimulus (Uchida et al., 2014, Haddad et al., 2013, Gill et al., 2020, Chong and Rinberg, 2018, Wilson et al., 2017, Smear et al., 2013, Smear et al., 2011, Shusterman et al., 2011, Cleland, 2014, Dalal and Haddad, 2022). The ubiquity of such patterns in MOS oscillations strongly suggests that they play important functional roles in chemosensory information processing. Yet, similar phenomena were not reported in the VNS.

One of the most notable differences between the MOS and the VNS involves stimulus uptake. In the MOS, stimulus uptake is linked to breathing, and active sampling modifies sniffing behavior and hence the manner by which information is relayed to downstream regions (Wachowiak, 2011, Verhagen et al., 2007, Kepecs et al., 2006). In contrast, VNS stimulus uptake is largely uncoupled from breathing, and instead relies on active suction by the vomeronasal organ (Meredith and O'Connell,

1979, Wysocki et al., 1980, Ben Shaul et al., 2010). Other differences between the two systems include the intrinsic properties of olfactory bulb neurons (Shpak et al., 2012, Zibman et al., 2011, Gao et al., 2017), their interactions with each other (Larriva-Sahd, 2008, Dulac and Wagner, 2006, Takami and Graziadei, 1991), and the properties of downstream regions that receive the information (Davison and Ehlers, 2011, Uchida et al., 2014, Haddad et al., 2013, Dalal and Haddad, 2022). Taken together, these observations imply that if, like the MOS, VNS information processing involves concerted patterns of population activity, they are likely to differ in their phenomenological expression and underlying mechanisms.

Previously, we and others (Tsitoura et al., 2020, Gorin et al., 2016, Zylbertal et al., 2017a, Zylbertal et al., 2015) have shown the occurrence of infra-slow oscillations in the AOB. In addition, a number of studies have shown a broad range of LFP AOB oscillations that can reflect experience, context, and potentially active arousal/sampling (Pardo-Bellver et al., 2017, Leszkowicz et al., 2012, Binns and Brennan, 2005, John et al., 2022, Tendler and Wagner, 2015). However, explicit relationships between these rhythmic population activity patterns and sensory stimulation and, more importantly, their potential interaction with single unit spiking activity, are not known.

Here, we describe prominent LFP oscillations in the AOB that conform to the theta frequency band. We show that these oscillations are induced by stimulus presentation and that their magnitude is stimulus-dependent. Notably, we find that, in addition to full-blown oscillations, the AOB network also displays a more subtle pattern of stimulus-dependent activity that closely resembles the oscillations in its spatial distribution. Our analysis supports a scenario in which, once sensory stimulation is sufficiently intense, these latent patterns develop into prominent oscillations. Based on their spatial and temporal features, we propose that these LFP patterns reflect a periodic exchange within the AOB network, likely involving AOB-MCs and GCs. Most importantly, we show that these oscillations constrain the spike timing of individual AOB neurons and can therefore serve as a thresholding, amplifying, and potentially also multiplexing mechanism. Thus, despite prominent differences in their constituent elements and their connectivity, it appears that, like the MOS, the VNS includes circuit elements that give rise to population level oscillations, which serve to orchestrate information transfer to downstream regions.

Results

To investigate LFPs associated with sensory processing in the AOB, we presented vomeronasal stimuli to anesthetized mice by direct application to the nostril, and electrically activated the VNO (**Fig. 1A**). In a typical experiment, we present each of multiple stimuli several times (typically 4-5) in a pseudorandom order (Yoles-Frenkel et al., 2017). During stimulus presentation, we record both LFP (0.5 – 300 Hz) and single unit activity using planar multielectrode arrays, which sample a substantial extent of the AOB. Our dataset contains recordings from 34 sessions in which LFP and single unit activity signals were recorded from adult anesthetized male and female mice. These recordings comprise different stimulus sets, electrode configurations, and penetration angles, and were conducted by several experimenters. Details about each session are given in **Table 1**.

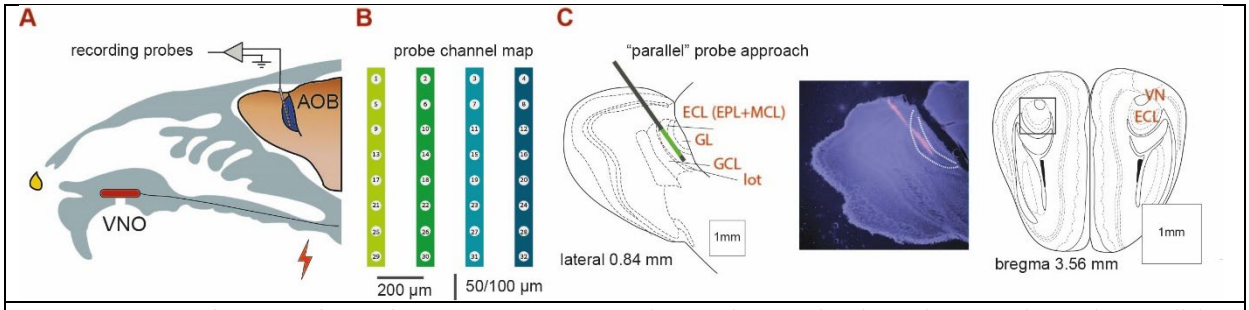

Fig. 1. Experimental setup and recording sites. A. Experimental setup showing the electrode array advanced in parallel to the AOB. The lightning bolt indicates stimulation of the sympathetic nerve trunk which innervates the VNO. During each trial, we apply a drop of stimulus (2 µl) to the nostril (application event) and, after 20 s, activate the VNO via a cuff electrode (stimulation event) placed around the sympathetic nerve trunk. After 40 s, we flush the nasal cavity and present another stimulus. See also **Fig. 2A**. **B.** Schematic of the 4x8 recording array. Inter-site distances along a single probe are 50 or 100 µM (see **Table 1** for details on electrode dimensions per session). **C.** Atlas images including the AOB in sagittal (left) and coronal (right) views. Images are taken and modified from (George Paxinos 2001). The black line in the sagittal section shows the approximate orientation of the recording probe. The green line shows the approximate extent of the recording region along one shank (with 100 µM inter-site spacing). The histological image shows the path of a DiI-stained probe (red), with nuclear DAPI counterstaining (blue). The broken white lines delineate the AOB ECL. The square within the coronal section shows the approximate horizontal extent of the probes (600 µM). ECL: external cellular later. EPL: external plexiform layer. MCL: mitral cell layer, GL: Glomerular layer. GCL: Granule cell layer. lot: lateral olfactory tract, VN: vomeronasal nerve layer.

<u>The AOB displays a spatially stereotypical pattern of oscillations</u>

To reveal notable LFP patterns in our recordings, we used a custom written data browser to manually scan multichannel LFP data. We first describe recordings made with 32-channel probes (see **Table 1**), which we advanced in parallel to the external cellular layer (ECL) of the AOB (**Fig. 1A-C**). This penetration angle was chosen to maximize the number of contact sites within the ECL, which contains cell bodies of AOB-MCs (Larriva-Sahd, 2008).

Browsing the data, we occasionally observed distinct oscillatory events (**Fig. 2A**). A prominent feature of these events is their characteristic amplitude distribution across channels. In order to analyze these events, and their relation to other experimental and physiological variables, it was first necessary to find an objective way to define them. This turned out to be a challenge since these events (as we show in detail below) varied in temporal and spectral characteristics. In addition, although their presence was often obvious (e.g., **Fig. 2A, B**), event onset and offset were typically gradual and thus difficult to delineate objectively. Finally, our experiments include inevitable sources of mechanical/electrical noise (associated with electric stimulation of the VNO, valve opening and closing, stimulus application, and rinsing of the nasal cavity) (Yoles-Frenkel et al., 2017), which may overlap with oscillatory events in the temporal and/or the spectral domains. These considerations imply that a simple bandpass spectral filter will yield both false positives and missed detections, and will thus not allow effective event detection.

To overcome these challenges, we exploited the fact that within a recording session, all events shared a similar across-channel envelope pattern. That is, while envelope amplitudes during these events often differed in *absolute* values, their *relative* amplitudes across recording channels were highly similar (**Fig. 2D**). This prompted us to use the average LFP envelope pattern across all manually defined events as a *template* (**Fig. 2E**), and use it to search for similar activity patterns across the entire recording session. Specifically, we calculate the linear correlation coefficient between the template and the LFP envelope across all channels at each point in time. The result is smoothed, rectified, and sharpened to increase contrast, yielding a measure of similarity between ongoing network activity and the oscillatory event template (see Methods for details). We denote this continuous measure as the *template match signal* (TMS) (**Fig. 2G**). The TMS for the data segment in **Fig. 2B** is indicated by the blue trace. Note in this example that the TMS is highest (close to 1) during the oscillatory episode

(shaded region), and very low during electric stimulation of the VNO. Notably, although the TMS decreases after the oscillatory event, it remains positive even after the oscillations have subsided, reflecting the relative distribution of LFP envelopes.

The TMS during an entire session is shown in **Fig. 2H**, with a time-expanded section in **Fig. 2I**. As a final step, we apply a threshold (see Methods) and use it to define discrete episodes with high TMS values (spanning at least 1 s). Automatically detected episodes are shown in the bottom panels of **Fig. 2H**, **I**. We stress that although there is an unavoidable level of subjectivity in this procedure, due to the manual selection of the seed events, once defined, the episodes are derived automatically and objectively. Furthermore, the high stereotypy between all user defined events (e.g., **Fig. 2D**) implies that the template, and hence the TMS, are minimally sensitive to the precise choice of manually defined events (see **Fig. S1** for an analysis of manual event similarity).

Importantly, the template itself is not only a useful construct for identification of network activity patterns, but also provides an indication of the *spatial* distribution of LFP magnitudes. When electrode channels are plotted according to their relative spatial locations, it is apparent that regions with high LFP activity correspond to a central active area, surrounded by a region with considerably lower magnitudes (**Fig. 2F**). As electrode positioning within the AOB is variable, the templates are distinct for each recording session, yet, almost all reveal a central hotspot of activity. Examples from different sessions are shown in **Figs. 2F** and **S2**. Considering AOB anatomy and probe dimensions relative to it (**Fig. 1C**), these patterns strongly imply that signals are locally generated, and do not represent volume conduction from other regions. Further evidence that supports local signal generation is provided in the following sections.

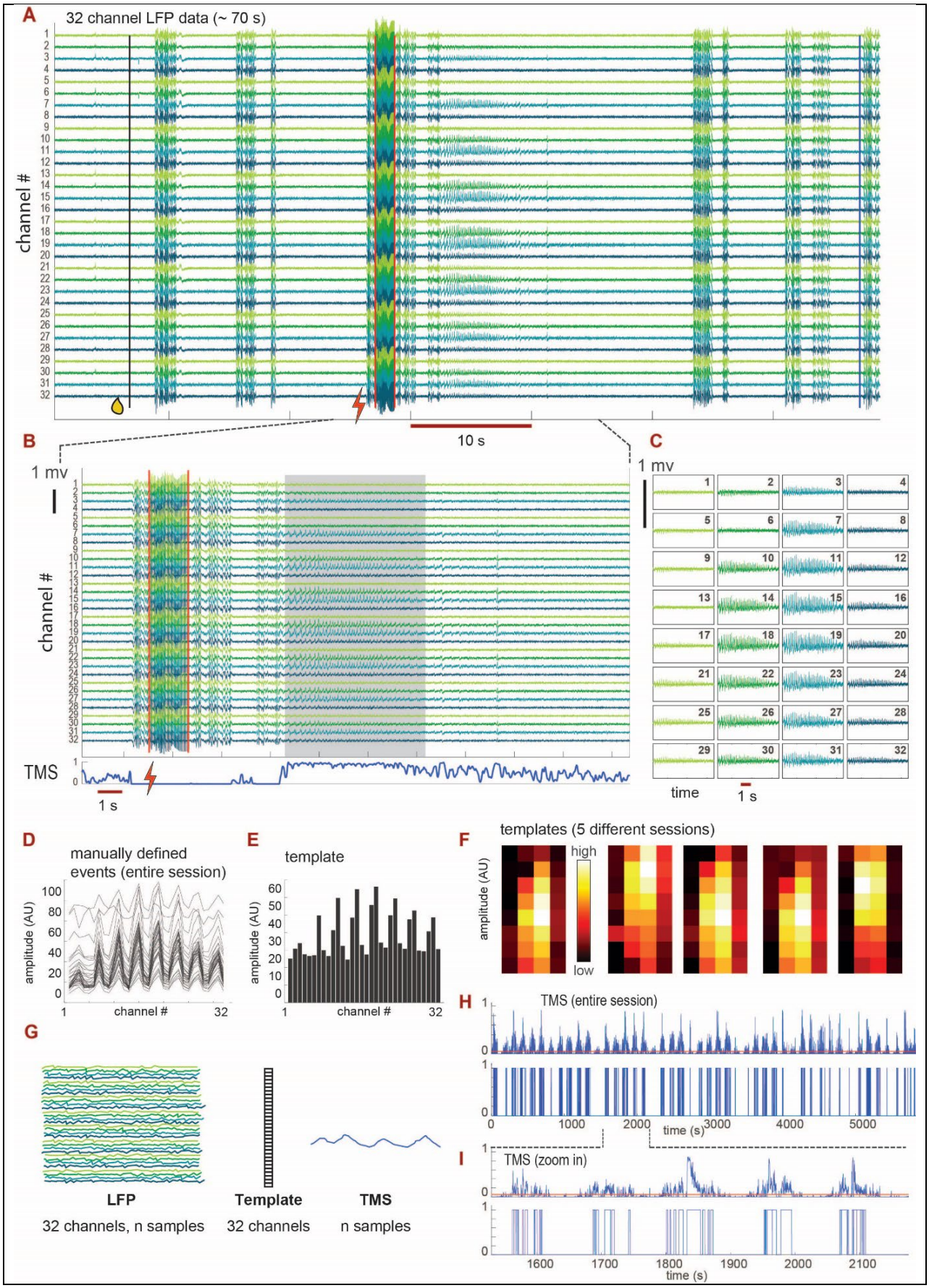
A
32 channel LFP data (~ 70 s)
channel #
10 s
B
1 mv
channel #
TMS
1 s
C
1 mv
time
1 s
D
manually defined
events (entire session)
amplitude (AU)
channel #
E
template
amplitude (AU)
channel #
F
templates (5 different sessions)
amplitude (AU)
high
low
G
LFP
32 channels, n samples
Template
32 channels
TMS
n samples
H
TMS (entire session)
time (s)
I
TMS (zoom in)
time (s)

Fig. 2. Basic analysis of the LFP data. A. LFP signals from 32 channels during one trial (~70 s). Stimulus *application* is indicated by the black vertical line and drop icon, VNO *stimulation* is indicated by the red vertical lines and the lightning bolt icon, and the rightmost vertical blue line represents the beginning of the wash period between trials. Channels are arranged according to their serial numbers (not spatial positions). Channel colors indicate the shank on which the recording site is situated (see **Fig. 1B**). LFP amplitudes are normalized to fit within the plot. A vertical distance of 1 on this plot (i.e., channel number baselines) corresponds to 357 µV. **B**. Zoomed-in section of A. The trace at the bottom shows the TMS for this data segment. Note that the TMS is high during the manually-defined oscillatory event (shaded rectangle), and low during the period associated with VNO stimulation and with other "noisy" time segments. Voltage and time scales are indicated by the bars. **C.** A section containing the oscillatory episode in B, with channels plotted according to their physical arrangement. In this session, horizontal distances (between shanks, columns) are 200 µm and vertical distances among sites are 100 µm. Channel numbers are indicated in each panel and correspond to the numbers in panels A-B and **Fig. 1B**. **D.** LFP envelopes (across all channels) associated with all manually defined events for the same session from which A and B are taken. **E.** The template for the session, derived by averaging the LFP envelope across all events in D. **F.** LFP envelope templates drawn spatially as a heat map (scaled to show the entire range). The leftmost image corresponds to the template in E. Templates for four other sessions are shown as well (see **Fig. S2** for more examples). **G.** Schematic overview of the TMS derivation process. See text and Methods for details. **H**. TMS (top) and binary above-threshold segments (bottom) during an entire session. **I**. Expanded scale of a section from panel H.

<u>The template match signal reflects sensory stimulation</u>

If the oscillations, and hence the TMS, are related to vomeronasal information processing, they should be modulated by sensory stimulation. Thus, we begin by investigating the relationship between the TMS and sensory stimulation. **Fig. 3A** shows an example of the TMS during an entire recording session, with epochs of stimulus presentation denoted by green horizontal bars. As can be seen from this image, the TMS essentially increases during all periods of stimulus presentation. However, the magnitude of the TMS varies from one presentation to another. This raises the idea that the network pattern reflected by the TMS varies as a function of the sensory stimulus.

To analyze TMS dependence on sensory activation, we derive its stimulus-triggered average (staTMS). For these analyses, we focus on one stimulus set, which includes 3 stimuli, each at 3 different dilutions (set D2 in **Table 1**). The global staTMS, based on all trials from all sessions are shown in **Fig. 3B**. The staTMS reveals that the TMS is tightly linked to stimulus presentation, first increasing during stimulus *application*, and further rising following electrical VNO *stimulation*. We note that this temporal profile is highly consistent with our previous observation that AOB neurons sometimes respond after stimulus *application*, prior to electrical activation of the sympathetic nerve trunk (Bergan et al., 2014, Bansal et al., 2021). The fact that full-blown oscillations often appear prior to electrical stimulation unequivocally demonstrates that they are not an artificial consequence of electric nerve cuff stimulation. Note that low TMS values during electrical stimulation (at 20 s, **Fig. 3B**) and at the trial end (60 s, start of wash period) result from the fact that the spread of noise energies is not correlated with that of the LFP energies during oscillatory episodes. Very similar results are obtained in another set of experiments using different stimuli (**Fig. S3**). In summary, these analyses indicate that the TMS is closely correlated with chemosensory stimulus processing in the AOB.

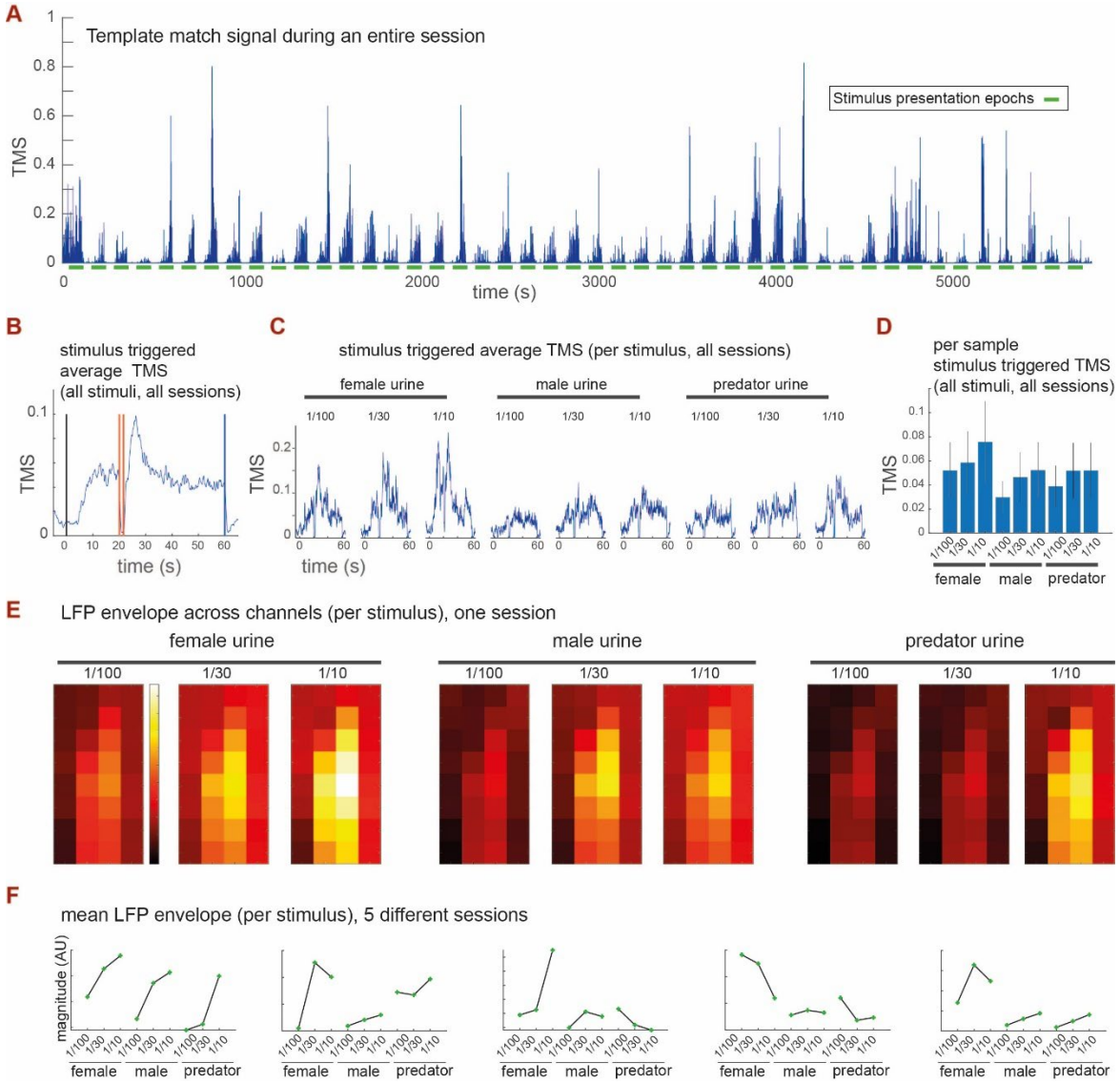

Figure 3. Stimulus dependence of the TMS and the LFP envelope. A. An example of the TMS during an entire recording session. Horizontal green lines correspond to stimulus presentation periods (60 s), starting with application to the nostril, and ending 40 seconds after nerve stimulation. Note that the TMS increases during stimulus presentation periods. **B.** Stimulus-triggered average TMS (staTMS), around all stimulus presentation times, in one type of experiment (D2, **Table 1**). Note how the signal rises following stimulus *application* (time 0), and then again during electric *stimulation*. The black vertical line corresponds to stimulus *application*. The two red vertical bars correspond to the start and end of the 1.6 s nerve stimulation. The blue vertical line marks the beginning of the wash period, which is effectively the end of the stimulation period. During electrical stimulation and wash, the TMS drops since electrodes record stimulation / flushing artefacts, respectively. **C.** Stimulus triggered average TMS (staTMS) for each stimulus. **D.** The mean template signal (directly proportional to the areas in C) and the standard error across all presentations of each of the stimuli. **E.** LFP envelope magnitudes associated with each of the stimuli. Note the stimulus and dilution dependence of the signal. **F.** Mean LFP envelope across all sessions in this type of experiment (D2, **Table 1**). Each panel shows values for one session. The leftmost panel corresponds to the data in E.

<u>Both the TMS and the LFP envelope depend on the sensory stimulus</u>

We have shown that the TMS rises during stimulus presentation, but is the TMS merely a reflection of stimulus uptake, or does it instead depend on the chemical composition of the stimulus? To answer this, we derived the staTMS separately for each stimulus (averaged across all sessions including the same stimulus set). Comparison of these staTMS reveal a stimulus-specific and dose-dependent response, with more concentrated stimuli eliciting higher staTMS profiles (**Fig. 3C**). Larger

responses to female than to male stimuli are also consistent with previous reports by us and others (Hendrickson et al., 2008, Bansal et al., 2021, Ben-Shaul et al., 2010). Despite notable variability across trials, comparison of TMS distributions across samples and sessions, averaged per stimulus, yields highly significant differences (**Fig. 3D**). Specifically, when comparing TMS value distributions using a Kruskal-Wallis test (across all samples, treated as independent samples), the p-value for a main effect of stimulus is essentially 0 (see Methods). Similar conclusions regarding stimulus dependence are reached when applying the same analysis to another stimulus set (**Fig. S3**).

Recall that the TMS is merely a measure of *similarity* to the energy distribution across channels during oscillatory epochs. Thus, high TMS values do not necessarily reflect high values for the LFP envelope itself. To test if LFP envelope *intensity* is also stimulus-dependent, we derived the average LFP envelope (considering time points during which the TMS was above threshold, as shown in **Fig. 2H, I**). An example of mean LFP envelopes in one session, for each of the 9 stimuli, plotted according to spatial location, is shown in **Fig. 3E**. This example shows that, like the TMS, the LFP magnitude (envelope) is also higher during presentation of less diluted stimuli. The mean LFP envelopes (averaged across the 32 channels) for all 5 sessions in this data set are shown in **Fig. 3F**. These examples show that in all of these sessions, the LFP magnitude varies with stimulus identity, and in many of them, also with stimulus dilution.

Taken together (and also see **Fig. S3**), we show that both the TMS, a measure of similarity to the LFP distribution during oscillatory events, and the LFP distribution itself, are stimulus dependent. Thus, more "intense" stimuli elicit stronger patterns, so that full-blown oscillatory episodes (like those shown in **Fig. 1B**) represent an above-threshold expression of an ongoing physiological activity pattern that is reflected by the TMS.

Stimulus-dependent spatial envelope distributions

Thus far, we have studied stimulus-induced changes in LFP *amplitude*, ignoring potential stimulus-dependent changes in *relative* intensity across channels. Indeed, the template matching approach implicitly assumes that a single template is applicable during an entire session. However, if the LFP envelope reflects computational processes within the AOB, then different stimuli might elicit distinct patterns, not only in magnitude, but also in spatial distribution. To paraphrase, one would expect stimuli with similar/diverse chemical compositions, to respectively elicit similar/diverse spatial distributions of the LFP envelope. To test this prediction, we compared the spatial distribution of LFP intensities for stimuli from the same source (at different dilutions) *versus* different sources (using sets D1 and D2, **Table 1**). This analysis (**Fig. S4**) revealed that, while the spatial LFP distribution is highly similar across stimuli, there is indeed evidence for subtle stimulus-specific spatial patterns. This is consistent with the notion that different stimuli activate different input and output channels (Hammen et al., 2014); see Discussion).

Analyzing the spectro-temporal characteristics of oscillatory episodes

Up to this point, we analyzed the TMS and showed its dependence on stimulus presentation. However, the TMS is not a physiological signal, but rather a continuous measure of similarity to the LFP envelope distribution that occurs during full-blown oscillations. In this section, we begin to analyze these oscillatory episodes directly. Because these episodes continuously vary in frequency (i.e., they present as amplitude and frequency modulated sweeps), we characterized them using a time frequency decomposition method. Specifically, we applied the wavelet synchrosqueezed transform (WSST), which is optimal for the analysis of time varying signals (Daubechies et al., 2011, Thakur et al., 2013). After applying the transform, we extracted time-frequency *ridges* from the transformed signal. The ridge extraction procedure yields multiple ridges with decreasing energy contributions. In our analyses, we only used the first ridge, i.e., the highest energy ridge. The inverse transform, inverse-

WSST (iWSST), can then be used to reconstruct the original signal from its time-frequency decomposition, or from one or more of the extracted ridges. A faithful reconstruction of the original signal using a single ridge indicates that the ridge provides a good account of the entire signal. This would be the case if the original signal is for instance an amplitude-modulated frequency sweep (e.g., a "chirp"), but not if the signal contains multiple simultaneously occurring frequency components (e.g., white noise). A major advantage of this ridge extraction procedure is that, at any given time point, a ridge has one dominant frequency component, allowing instantaneous phase derivation using the Hilbert transform.

Fig. 4A-D shows an example of the application of this procedure to one channel during one oscillatory episode. The original signal (black) and its reconstruction (green) are shown in **Fig. 4A**. The frequency (blue) and amplitude (green) of the first extracted ridge are shown in **Fig. 4B**, and the instantaneous phase is shown in **Fig. 4C**. **Fig. 4D** shows the original signal in the time domain (white), and the spectrogram of the first ridge. To assess reconstruction quality provided by the first ridge, we calculate a reconstruction score as the correlation coefficient between the original signal and its one-ridge reconstruction. To characterize the frequency, we calculate the (amplitude-weighted) mean frequency along the first ridge (see Methods). For the episode shown in **Fig. 4A-D**, the reconstruction score is 0.84 and the mean frequency of the first ridge is 5.25 Hz, clearly within the conventional theta frequency range.

<u>Oscillatory episodes are often frequency sweeps within the theta range</u>

To analyze the frequency characteristics of the oscillatory episodes, we applied the above procedure to all data segments for which the TMS was above threshold (e.g., **Fig. 2H, I**, bottom) for at least 1 s. For each episode, the analysis was applied to the channel with the maximum (mean) LFP envelope (see also **Fig. S9**). After applying the transform, we derived the reconstruction score and the mean frequency associated with that first ridge, as described above. We then retained episodes for which the mean frequency of the first ridge was within the theta range (2-14 Hz), and which yielded a reconstruction score > 0.5. These selection criteria were applied to exclude episodes without a dominant theta band component. The 2-14 Hz range was chosen based on manual inspection of oscillatory episodes, which were all within the range. Finally, we visually monitored each and every episode to exclude "false positives" (episodes whose high reconstruction score is not due to a dominant theta mode), and conversely, identify "complete" episodes: episodes that contain an entire oscillation event from start to end without interruption. Of 2609 candidate episodes, 266 were designated as false positives and thus excluded from further analysis, while 89 were designated as complete. Examples of ten such episodes are shown in **Fig. 4E**. These examples underscore the diversity in oscillatory episode duration and frequency content. While many episodes show a smooth up and down sweep in the frequency domain, others show a less regular structure. Similar plots for all *complete* episodes and their first ridge reconstructions are shown in **Fig. S5**.

Fig. 4F shows the relationship between the mean TMS and the reconstruction score for all episodes (excluding false positives), with complete episodes highlighted in red. It can be seen that episodes with higher TMS values generally yield better first ridge reconstructions. The relationships between the TMS, ridge frequency, LFP envelope, and reconstruction scores across all episodes are shown in **Fig. S6**. **Fig. 4G** depicts the distribution of mean frequencies (7.1 Hz) and durations (2.29 s) across all episodes (n = 2343). **Fig. 4H** shows these data for complete episodes (n = 89, average frequency: 5.47 Hz, mean duration 5.16 s). Note that, in both cases, mean frequency distributions peak well within the cutoff range (2-14Hz).

In conclusion, this analysis shows that although the oscillatory episodes fall within the theta range, individual episodes can assume various forms, in both their duration, and in their time frequency characteristics. Notably, there are also clear differences in episodes recorded *within* a single

session (the ten episodes shown in **Fig. 4E** were recorded in two different sessions, see **Fig. S5**), indicating that variability is not merely a consequence of different experimental preparations or electrode positioning.

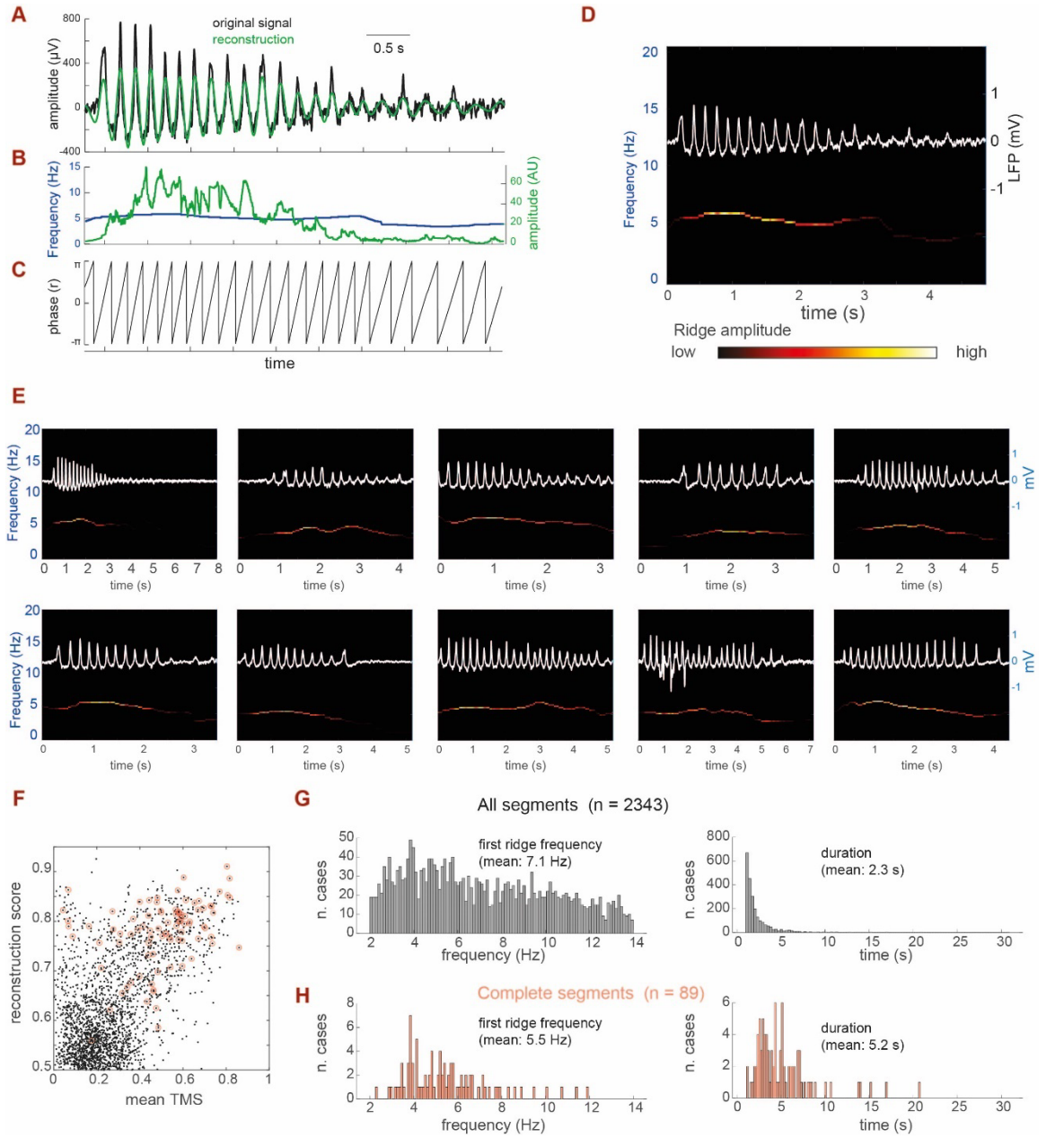

Fig. 4. Spectral analysis of oscillatory episodes. A. An oscillatory event in one channel showing the original signal (black) and its reconstruction from a single ridge (green). **B.** Time evolving frequency (blue) and amplitude (green) of the first ridge. **C.** Instantaneous phase of the first ridge. **D.** The original signal and the first ridge spectrogram. In this representation the ridge amplitude (green trace in panel b) is indicated by heatmap color. **E.** Spectral analysis of ten oscillatory episodes, using the same representation as in panel D. The same vertical axes are used for all episodes, but horizontal (time) scales vary. Note that many of the episodes shown an increase and then a decrease in frequency. All episodes on the top row and the first episode on the left in the bottom row are from the same session, as is the episode shown in panel D. The other episodes are all from another session. **F.** Relationship between mean TMS and the reconstruction score for each of the episodes. Episodes designated as complete are highlighted with red circles. **G.** Distribution of (mean) first ridge frequency and duration for all episodes. **H.** Distribution of (mean) first ridge frequency and duration for all complete episodes.

Oscillations are most prominent in the ECL and likely reflect a reciprocal exchange between AOB-MCs and GCs

We next turn to investigate the network source of the oscillations. Most recordings (see **Table 1**) were conducted with the planar electrode array advanced *in parallel* to the AOB ECL (**Fig. 5A**), also denoted as the mitral cell layer or external plexiform layer (Larriva-Sahd, 2008). The ECL contains the cell bodies of AOB-MCs and displays characteristic signatures of spiking activity (Ben Shaul et al., 2010, Luo et al., 2003). Although we dip electrodes in a fluorescent dye to routinely confirm within-ECL location *post-hoc*, reconstructions are never accurate enough to assign individual contact sites to specific layers. However, we gain important information about electrode localization by comparing hotspots of single unit neuronal activity with LFP energy distributions in each recording session. An example of correspondence between LFP signals and unit activity is shown in **Figs. 5B** and **5C**, respectively. These qualitative analyses show clear correspondence between oscillatory LFP power, neuronal firing activity, and often, stimulus-induced neuronal responses (not shown).

If the LFP waveforms measured during parallel penetrations originate from the same neuronal structure, the oscillations are likely to be in-phase, without reversal of polarity. **Fig. 5E** shows all LFP channels during one oscillatory episode from the session shown in **Fig. 5B, C**. The same episode is shown in expanded time view in **Fig. 5F.** This representative example shows that all channels within a session are indeed in-phase, supporting the notion that they originate from a homogenous neuronal structure (see **Fig. S7** for another example from another session).

Continuing this line of reasoning, if oscillations result from an exchange between neuronal elements in different AOB layers, then their polarity should reverse at some level. To address this possibility, in a subset of experiments (see **Table 1**), we advanced electrodes *perpendicular* to the AOB, to span its different layers (**Fig. 5G**, also showing a dye tract of the electrode shanks in one such recording**).** Indeed, in most of these perpendicular penetrations, we observe a clear LFP reversal at deeper, compared to superficial sites. Because this is a crucial point, we provide examples from three different sessions (**Fig. 5H-J, K-M, N-P**). The simplest interpretation of this reversal is that it represents the transition along the lateral olfactory tract, which separates the ECL from the AOB granule cell layer (GCL). Consistent with the idea that the AOB GCL activity is typically not detected by extracellular recordings, we observe neuronal spiking activity above, but not below the reversal (**Fig. 5I, L, O**).

Further support for our hypothesis that LFP reversals represent the transition between ECL and GCL is gained from current source density (CSD) analysis. CSD is the second derivative of the electric potential with respect to position, and provides a measure of current sources and sinks (Mitzdorf, 1985). We apply this analysis along the length of the recording electrodes which contain equally spaced recordings sites (and ignore the spread between adjacent electrodes). The CSDs along the sites of LFP polarity reversals (denoted by the shaded regions in **Fig. 5 H, K, N**) are shown in color, superimposed on the original LFP traces in **Fig. 5Q**). CSD plots reveal an exchange of sinks and sources within each cycle period. Most importantly, the CSD itself shows a reversal along the AOB layers that matches the LFP reversal. As explained in the Discussion, this interpretation is further supported by previous descriptions of LFP and CSD in AOB slices (Jia et al., 1999), and leads us to propose that oscillations reflect a reciprocal exchange between AOB-MCs and GCs.

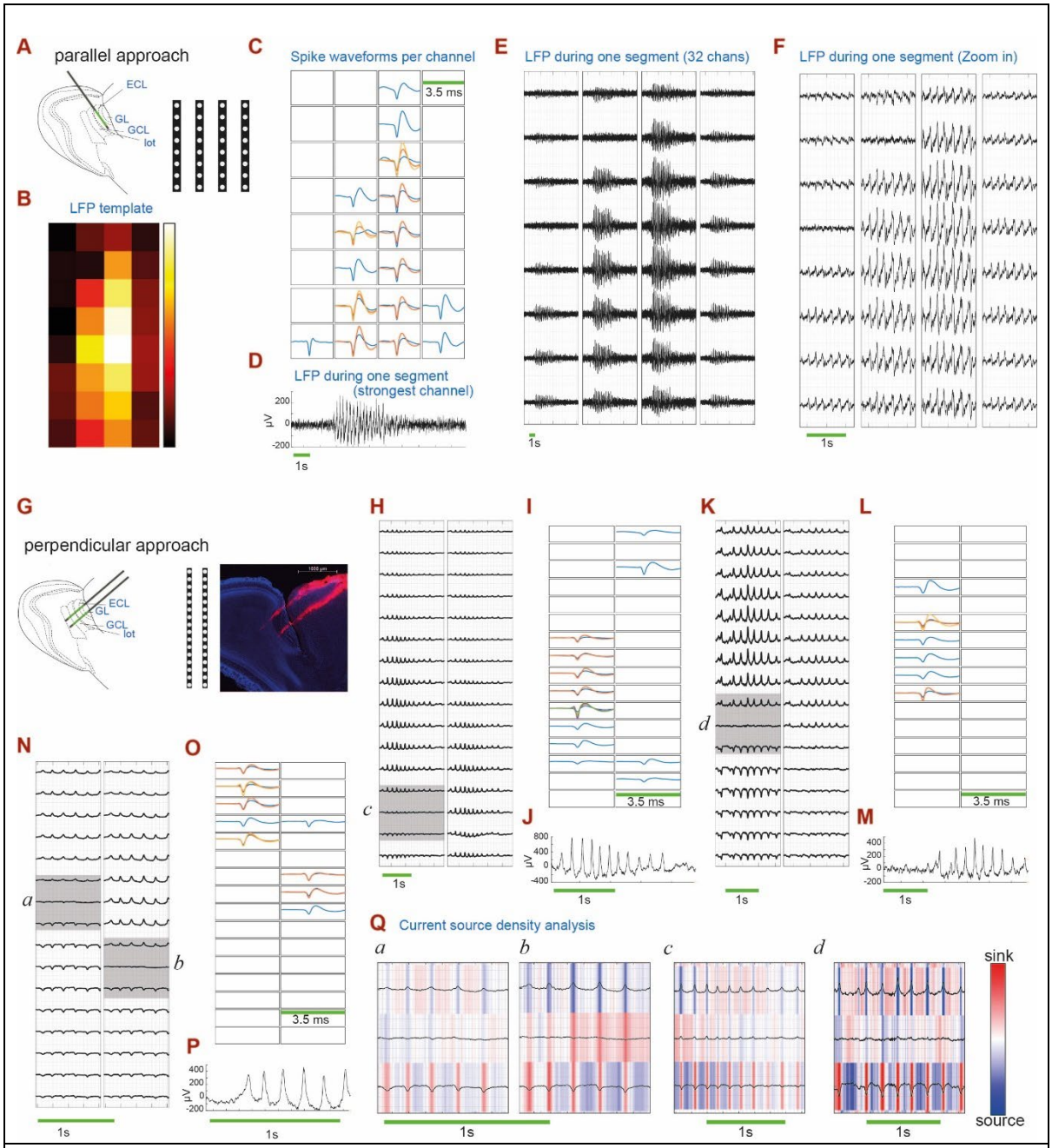

Fig. 5. Evidence for localization of oscillations within the AOB ECL. A. Schematic of a parallel penetration into the AOB. **B.** Spatial spread of LFP energies in one of the sessions (also shown in **Fig. 1**). **C**. Spike waveforms in the sites shown in A. Each square shows the spike waveforms recorded in that channel. Both single unit and multi-unit activity waveforms are shown. Each trace in each panel corresponds to one single-unit or multi-unit. Although a given neuron can be recorded by multiple channels, here, we plot the waveform on the channel in which it had the largest amplitude. Note the correspondence between spiking activity and LFP amplitudes. **D.** Recording from one channel during an oscillatory episode. Shown is the channel with the maximal amplitude. **E.** LFP oscillations during the episode shown in the previous panels, across all channels, plotted according to spatial position. **F.** Magnified temporal view of E, highlighting the phase similarity across all channels. **G**. Schematic of a perpendicular penetration into the AOB, using probes with a 2x16 configuration. Also shown is a dye tract of the electrodes in the session shown in panels H-J. **H.** LFP amplitudes on the 2x16 electrode array. Note the reversal of the LFP along the probe (shaded regions). **I.** Spike shapes recorded on the sites shown in H. **J**. Close-up view of the channel with maximal amplitude in H. **K-M**, like H-J for another session. **N-P,** like H-M for yet another session. Note in I, L, and O that spiking activity is confined to sites above the LFP reversal. **Q**. CSD analysis of the areas indicated by gray squares in H, K, and N. The relevant sections are indicated by the italicized letters. These CSD plots illustrate periods with reciprocal change between sinks and sources around the reversal point. Temporal scales in all plots are indicated by the green horizontal bars.

Relationship between LFP oscillations and single unit activity

How is the LFP signal related to AOB unit activity? In this section, we begin to analyze the relationship between both physiological signals. The TMS and the summed rate (combined across all recorded single and multi-units) during an entire session are shown in **Fig. 6A**. Clearly, at this coarse time scale, the two signals are correlated, as expected since both are modulated by stimulus presentation. Yet, inspection of the relationship at a finer temporal resolution reveals that the signals do not overlap precisely (**Fig. 6A** bottom).

To obtain a quantitative measure of their temporal relationship, we calculated the cross covariance (CC) between the TMS and unit activity, both for the summed spike rate across all units (within a session) and for each (single) unit individually. Specifically, we derived the maximum CC, and the lag at which it was obtained. For the summed rate signal in each session (**Fig. 6B**), both CCs and lags are generally positive, indicating that the TMS precedes the unit signal (n = 34 sessions, median CC: 0.1449, sign rank p-value (of the null-hypothesis that medians are 0): $1.6 \bullet 10^{-05}$, median lag: 0.394 s, sign rank p-value: 0.0007). A similar result is obtained considering each single-unit individually (**Fig. 6C,** n = 520 units). Here, however, the lag distribution is more symmetrical around 0, with many units showing negative lags for the maximal CC. In this case, the median CC is 0.067 (sign rank p-value: $1.03 \bullet 10^{-42}$) while the median lag is 0.247 (sign rank p-value: 0.002).

To obtain a more accurate estimate of the relationship between the signals around stimulus presentation, we superimposed, for each session, the staTMS and the single-unit-summed peri-stimulus time histogram (summed-PSTH). Examples from eight different sessions are shown in **Fig. 6D** (see **Fig. S8** for additional examples). Despite session-to-session variability in both signals, we can draw several conclusions. First, the TMS is generally a more reliable indicator of sensory stimulation. This is expected since single unit sampling is sparser and more random, with marked differences in yield across sessions. This highlights the relevance of the TMS as a simple and reliable measure of stimulus-induced VNS activity. Second, in most cases, both signals peak at a similar time. Finally, the comparison also shows that the TMS has a sharper onset and offset as compared to the summed-PSTH. However, recall that TMS derivation includes a contrast-enhancing step, which limits the interpretation of such a comparison.

Based on the above observations, we propose the following scenario: VNO activation gives rise to spiking activity of single AOB neurons. With sufficient single unit activation, the network starts to recruit GCs, which supply inhibitory feedback to AOB-MCs and entrain oscillations. These oscillations then persist as long as incoming inputs provide sufficiently strong drive to AOB-MCs. Once AOB-MC firing rates drop (due to reduction of incoming inputs), reduced GC activity is no longer sufficient to drive oscillations. According to this scenario, full-blown LFP oscillations represent the climax of stimulus-induced AOB activity. This scenario is consistent with the observation that oscillatory episodes (see **Fig. 4E, G, H** and **Fig. S5)** are briefer than response times of many individual AOB single units (Yoles-Frenkel et al., 2018).

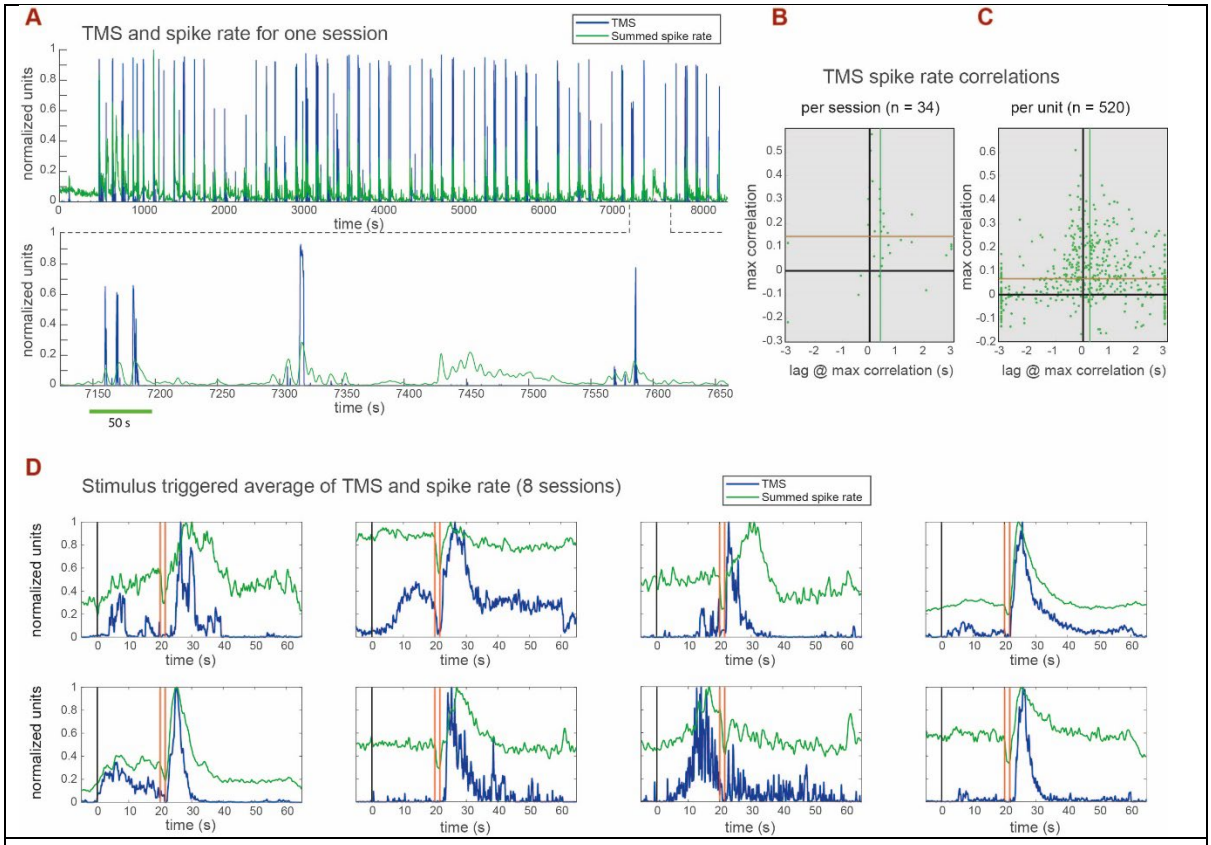

Fig. 6. Relationship between TMS and unit activity. A. LFP template match (blue) and summed neuronal activity signal (green) during an entire session. A magnified view is shown below. Although the signals are correlated by virtue of their stimulus dependence (correlation of 0.565 at a lag of 0.076 s), a closer examination shows that they are not always overlapping. Both single and multi-unit data are included in the green traces in this panel. **B**. Maximal cross covariance magnitudes and the lags at which these CCs were obtained, for the summed unit activity signal in each session. The medians of the distributions of CCs (red lines) and lags (green lines) are both positive. **C**. As in B, but here each dot represents one single unit. Although there is a spread of lags, usually the highest CC is achieved when unit activity is delayed with respect to the LFP signal. **D.** Stimulus triggered averages of the TMS and the summed single unit activity (PSTH). Averages of both measures were calculated across all stimuli in each session. Green and blue traces correspond to the summed single unit PSTH and the TMS, respectively. Each of the eight panels represents one session. See **Fig. S8** for further examples.

Relationship between neuronal firing times and the LFP phase

In various brain regions and systems, and in the MOS in particular (Kay, 2015), LFP oscillations can reflect orchestrated action potential timing of individual neurons (Buzsáki, 2006). For example, in the MOB, constrained spike timing can facilitate activation of downstream brain regions, or multiplex information in individual channels (Cury and Uchida, 2010, Uchida et al., 2014, Shusterman et al., 2011, Smear et al., 2011, Fukunaga et al., 2014). We now investigate whether a similar mechanism may be at play in the AOB as well. Specifically, we study the relationship between spike timing and the LFP phase.

To determine the instantaneous LFP phase at each time point, we applied the Hilbert transform (see Methods and **Fig. 4C**). Recall, that we only consider oscillatory episodes for which the first ridge was within theta (2-14 Hz) range, and that also yielded a reconstruction score > 0.5. Critically, the phase is derived from the channel with the highest LFP energy. This could be a concern if different channels displayed varying phase lags with respect to each other, so that a single channel would not be representative of all. Although the examples in **Figs. 5** and **S7** already suggest that all channels are in-phase, we also tested and confirmed this assumption quantitatively (see **Fig. S9**).

Having assigned a phase to each sampling point, and hence to each action potential, we can address several hypotheses. In all following analyses, we compare the distributions obtained with the

real data to those obtained with phase-shuffled data (see Methods). First, we tested if the population of single units displays phase distributions that deviate from uniformity, using the omnibus test for uniformity of circular data (Berens, 2009). **Fig. 7A** shows examples of phase distributions (green bars) of eight single units with significant deviations from uniformity. The lighter gray bars within each panel show the phase distributions of the LFP phases across the entire recording session (which are expectedly, flat). Under the null hypothesis that spike timing is independent of the LFP phase, the distribution of p-values (for deviations for uniformity) across the population should itself be uniform, and the cumulative distribution should follow the diagonal. As shown in **Fig. 7B**, this is not the case. There is a marked excess of small p-values for the real, but not for the shuffled data. The probability of obtaining such an excess of small p-values (e.g., smaller than 0.05) can be calculated with the binomial distribution (see Methods), and is extremely small (n = 331 single units, probability under binomial model: $3.9 \bullet 10^{-36}$). This corresponding p-value distribution for the shuffled data is uniform, without evidence for excess of small p-value (binomial p = 0.90). We note that (as expected) shuffled p-values slightly change each time the analysis is run, but our conclusions remain entirely valid across many repeated runs. Thus, our first conclusion is that as a population, AOB-MCs display spike time preference with respect to the LFP phase.

Next, we consider the distribution of the preferred (i.e., circular mean) phases of the units. Under one extreme scenario, preferred phases homogeneously tile the LFP cycle period, resulting in a uniform distribution of preferred phases. At the other extreme, all units share similar preferred phases. Examination of the actual preferred phase distribution (**Fig. 7F**) again shows a clear deviation from uniformity (N = 331, mean phase: 207 degrees, omnibus test for uniformity $p = 4.8 \bullet 10^{-27}$). Very similar results are obtained when considering only single-units with a significant deviation from uniformity (**Fig. 7G**, n = 84, probability under binomial model: $1.3 \bullet 10^{-11}$ mean phase: 203 degrees). Notably, preferred phases correspond to the negative LFP phase, which is consistent with a current sink in the ECL. When considering shuffled data (**Fig. 7H**), preferred direction distributions do not deviate from uniformity.

Importantly, despite the spread of spike time phases of individual units (**Fig. 7A**), many pairs of units show distinct phase distributions. This is revealed through pairwise comparisons of phase distributions among simultaneously recorded units, using a non-parametric multi-sample test for equal medians (Berens, 2009). The analysis (**Fig. 7C**) shows a marked excess of significant differences (n = 1560 unit-pairs, probability to obtain such an excess of p-values < 0.05 under the binomial model: $1.18 \bullet 10^{-85}$, for the shuffled data: p = 0.038). We note that, although the probability for the shuffled data is smaller than 0.05, the corresponding probability for the real data is orders of magnitude smaller (see Methods for further explanation / discussion). We therefore conclude that along with the clear deviation from uniformity and the preference for the negative phase of the LFP cycle, there are frequent significant differences between LFP phase distributions of unit pairs.

Finally, we test a more elaborate hypothesis, according to which individual units show distinct phase distributions when different stimuli are presented. First, we consider the population of unit-event pairs and ask, as before, whether there is an excess of small p-values (under the null hypothesis of uniform distributions). This analysis (**Fig. 7D**) shows that this is indeed the case for the real (n = 743 unit-event pairs, probability under the binomial model: $3.04 \bullet 10^{-15}$), but not for shuffled data (p = 0.99). Second, we compare phase distributions of the same unit for two different stimuli. As shown in **Fig. 7E**, there is indeed a marked excess of significant pairwise differences for the real data (1675 comparisons, probability under the binomial mode: $9.36 \bullet 10^{-23}$), but not for the shuffled data (p = 0.03). This analysis is thus consistent with the idea that a given unit may exhibit distinct phase distributions, depending on the sensory stimulus which elicited the oscillations.

Taken together, we have demonstrated various forms of non-uniform phase distributions which can play important roles in information transfer to downstream regions. We address these roles in the Discussion.

The effects of phase-dependent firing markedly increase with neuronal population size

One might get the impression that, despite their significance and prevalence, the degree of phase locking observed here (e.g., **Fig. 7A**) does not suffice to induce a substantial effect on downstream neurons. However, while deviations from uniformity of individual neurons are arguably modest, such deviations add up and can become extremely meaningful when considering co-active neuronal *populations*. A simple calculation illustrates this point. Adopting the perspective of a downstream integrating neuron receiving a certain number of inputs, we can calculate the probability to obtain a particular number of spikes within a specific integration window. We compare this probability between a uniform and a non-uniform probability of firing within a cycle, keeping the overall firing probability constant. For example, we can consider neurons firing at a constant rate of 5 Hz throughout the cycle, to neurons that fire at 4.5 Hz within one half of a cycle, and at 5.5 Hz during the other half (i.e., during the negative phase of the LFP). We can then calculate the probability to obtain a certain number of spikes within a particular part of the cycle (e.g., the negative phase of the LFP.

More specifically, we ask how the probability to obtain a given number of action potentials within such a window depends on the firing rate of each neuron within the window, and the number of neurons in the population. This probability can be calculated using the binomial cumulative density function (see Methods). As shown in **Fig. S10**, the differences, which increase with population size and the extent of phase locking, can be dramatic. For example, consider a population of 50 neurons, an integration window of 100 ms (half of a 5Hz theta cycle), and a baseline probability of 5 Hz (uniform firing) compared to a mildly locked non-uniform distribution (50% increased probability = 7.5 Hz within the window). Under these conditions, the probability to observe 30 spikes within that window is 0.14 under the uniform distribution, and 0.88 with the phase locked distribution. This is a probability difference of 0.74, and a factor larger than 6. In other words, under these conditions, a mild degree of phase locking can increase the probability of observing 30 spikes within a 100 ms window 6-fold! Considerably larger differences can be attained with higher degrees of phase locking and larger neuronal populations (**Fig. S10**). This simple calculation serves to show that a relatively modest degree of phase locking can exert profound effects on downstream neurons if the relevant population is sufficiently large.

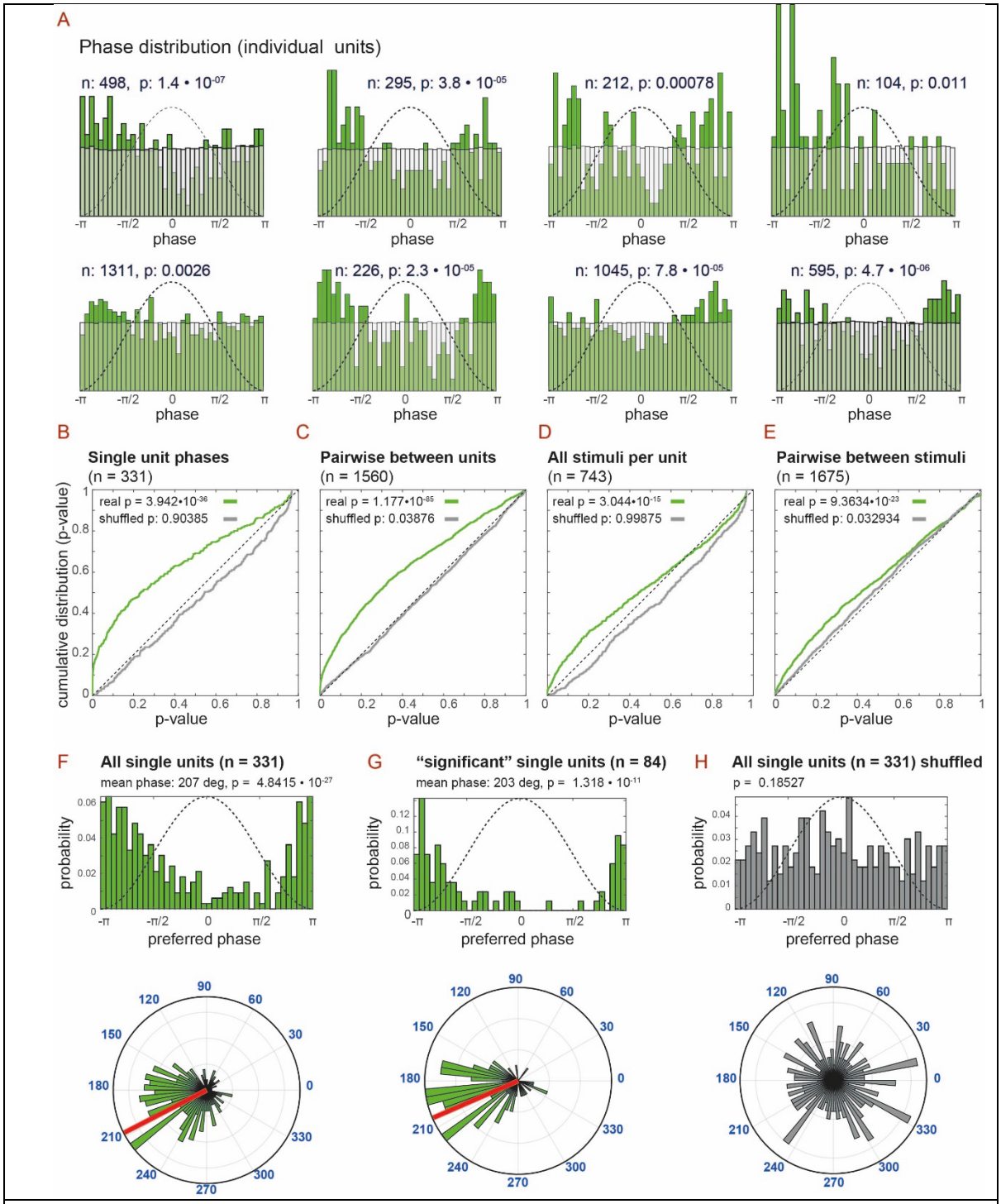

Fig. 7. Distributions of single unit spike times relative to the oscillation phase. A. Phase histogram of 8 different single units; number of spikes and p value for tests of uniformity are indicated in each panel. The broken line represents the LFP oscillation as a reference. Green bars show the units' phase distribution. Lighter bars show the distributions of the LFP phases across all episodes during the corresponding recording session, and are flat as expected. **B.** Cumulative distribution of p values for the test of uniformity (of spike times relative to LFP phase) across all single units. Green and gray traces correspond to real and shuffled phase data, respectively. **C.** Cumulative distribution of p values for pairwise comparison of phase medians across all simultaneously recorded unit pairs. **D**. Cumulative distribution of p values for each unit and stimulus combination. **E.** Cumulative distribution of p values for pairwise comparison of phase medians across all stimulus pairs per unit. Note that for the analysis in **D-E** we only consider unit stimulus combinations for which there are at least 50 spikes. **F.** Preferred phase distributions across all single units and **G**. single units with a significant deviation from phase uniformity ($p < 0.05$), shown in both linear (top), and polar (bottom) histograms. The red bars in the polar plots show the mean phase. Broken lines in linear plots shows the LFP cycle for comparison. **H:** Like panel F, but for phase shuffled data.

Discussion

In this manuscript, we studied oscillatory LFP patterns in the AOB. While spiking activity is probably the most instructive measure of the information relayed between neurons, LFPs can reveal population level processes that are not easily observed by the activity of (even many) single units. We provided evidence that LFP oscillations are generated locally within the AOB, are associated with stimulus sampling, and occur even in the absence of arousal or active investigation. We have shown that they fall within the theta band, but their sporadic appearance indicates that they are distinct from breathing-associated theta band oscillations in the MOB. Most importantly, we have shown that these oscillations exert a marked influence on neuronal spike timing, which can have profound effects on downstream integrating stages. We thus propose that these oscillations play an essential role in shaping AOB outputs that are relayed to various processing stages to control behavioral and physiological processes.

The template matching approach

We discovered these sporadic theta oscillations by manually browsing LFP data. While often they were obvious, sometimes they were weak and obscured by noise associated with various mechanical and electrical events that our experiments involve. These intrinsic and technical constraints impeded a systematic analysis of the relationship of these oscillations to stimulus presentation and to unit activity. To overcome this challenge, we developed a semi-automatic method to identify oscillations. Our approach relies on the highly conserved nature of envelope distributions within a recording session (**Figs. 2D, S1**). Using the mean energy distribution as a template, we search for similarity throughout the recording session, thereby generating the continuous TMS. Initially, we expected the TMS to specifically capture bona-fide oscillatory episodes. However, we found that in most recording sessions, it waxed and waned during the entire session, with a clear correspondence to periods of stimulus presentation (see **Fig. 3A, B**), and to its identity (**Fig. 3C-F**). Thus, the TMS provides a measure of stimulus related network activity, with peaks representing full-blown oscillations following efficient recruitment of the AOB network. On a practical note, the TMS, which is sensitive to the spatial pattern of activity, provides a reliable way to monitor stimulus-induced activity in the AOB (and, potentially, other regions as well). LFP signals are considerably easier to record than single-unit activity and, thus, a small number of electrodes sampling LFP activity in the AOB can provide a reliable readout of sensory activation.

Source of the oscillations

The reversal of the LFP signal, and its comparison with the spread of unit activity (**Fig. 5**) led to the conclusion that the origin of the oscillations is the AOB ECL. In addition, important insights can be gained from previous work in AOB slices. Specifically, Jia et al. (Jia et al., 1999) recorded LFP signals in different AOB layers during vomeronasal nerve activation. Based on LFP waveforms and CSD analysis, stimulation-induced LFP signals were divided into three periods. The first, strongest in vomeronasal nerve and glomerular layers, was attributed to activation of presynaptic vomeronasal sensory neuron axon terminals. The second period included a current sink in the glomerular layer and a source in the ECL. This sink/source pair was attributed to depolarization of apical AOB-MC dendrites. In the third period, a large sink appeared in the ECL with a corresponding source in the GCL. The authors attributed the ECL sink to GC peripheral dendrite depolarization, which can be induced by synaptic activation of AOB-MCs. Using whole-cell recordings from AOB-MCs and GCs, Jia et al. observed that the second LFP period coincided with excitatory post synaptic potentials in AOB-MCs, that evolved into action potentials. In the third period, inhibitory post synaptic potentials appeared in AOB-MCs, along with excitatory potentials in GCs. This inhibition was associated with reduced AOB-

MC action potential generation. Put simply, the three phases correspond to sequential activation of three main AOB circuit elements: vomeronasal nerve layer, AOB-MCs (which span the glomerular layer and the ECL), and GCs (which span the ECL and the GCL). Based on our observations and the detailed analysis by Jia et al., we propose that the oscillations observed here result from ongoing AOB activation, which, if sufficiently strong, leads to reciprocal exchange between AOB-MCs and GCs. We speculate that stronger incoming activation not only increases the rate of AOB-MC activation, but also that of GCs, resulting in higher charging slopes and oscillatory frequencies. As the incoming signal wanes, there is no longer sufficient drive to activate AOB-MCs and GCs in synchrony, and oscillations decelerate and, eventually, disappear. Thus, the varying frequencies observed within a single oscillatory episode may be due to changes in the extent of incoming activation of AOB-MCs. Furthermore, different AOB-MCs may have different temporal response features (Yoles-Frenkel et al., 2018), and thus changes in temporal LFP signal features can result from changes in specific subsets of active AOB-MCs. It is important to note that, while these AOB oscillations fall within the theta band, they are mechanistically distinct from MOB theta oscillations (Kay, 2014). Since all our experiments were conducted in anesthetized mice, and most of them included tracheotomy, we conclude that the oscillations are triggered by sensory activation and are not dependent on active exploration or feedback from other areas. In a few experiments (see **Table 1**), a tracheotomy was not performed (and there was also no flushing of the nasal cavity). Also in these experiments, we did not observe ongoing breathing-associated theta oscillations, further supporting the claim that breathing does not play a direct role in the oscillations studied here.

Stimulus identity-dependent LFP envelope distributions

We have shown (**Fig. S4**) that the LFP envelope may reflect stimulus identity and not merely its intensity. In fact, given that different stimuli activate different subsets of sensory neurons and glomeruli, one might expect even higher differences among envelopes elicited by stimuli from distinct sources. The relatively small differences (i.e., high correlations) may result from (***i***) the fact that our stimuli are mixtures with potentially significant overlap in components, (***ii***) the distributed nature of vomeronasal sensory neuron axons within the glomerular layer (Dulac and Axel, 1998, Dulac and Axel, 1995), and (***iii***) the broad sampling of the glomerular layer by AOB-MCs (Takami and Graziadei, 1991). Consistent with these considerations, our previous observations also indicate that a large proportion of AOB-MCs respond to a broad range of stimuli (Bergan et al., 2014, Ben-Shaul et al., 2010). Given these considerations, it will be interesting to compare LFP patterns elicited by more distinct stimuli (i.e., with less chemical overlap), and examine if they show more differences than observed using the present stimuli.

Previous studies on AOB theta oscillations

Our study of theta band LFP oscillations in the AOB follows previous reports of this phenomenon. In addition to the *in vitro* analysis mentioned above (Jia et al., 1999), work from the Brennan (Binns and Brennan, 2005, Leszkowicz et al., 2012) and Lanuza laboratories (Pardo-Bellver et al., 2017) revealed stimulus-induced theta band oscillations in the AOB (see Figure 1 in (Binns and Brennan, 2005) and Figure 2 in (Lanuza et al., 1996)). The former study also showed that oscillatory LFP bands can change as a result of mating experience. Recordings in rats (Tendler and Wagner, 2015) revealed that coherence among theta LFP in various limbic regions (including AOB) depends on behavioral context. This broad distribution of theta oscillations throughout limbic regions suggests that the patterns observed here may induce, or resonate with downstream VNS regions. While our recordings show that oscillations can arise in the absence of arousal, the work of other groups highlights the relevance of oscillations in the freely moving state.

Another prominent class of AOB oscillations, described by us and others, are infra-slow oscillations (Gorin et al., 2016, Tsitoura et al., 2020, Zylbertal et al., 2017a, Zylbertal et al., 2017b). Those oscillations are much slower than those observed here, likely play a different role, and arise from distinct mechanisms. Nevertheless, there may be a direct relationship between neuronal ensembles such as identified in (Tsitoura et al., 2020) and those that we propose here (see below and **Fig. 8**).

Mechanisms underlying generation of the oscillations

Mechanistically, we proposed that AOB theta oscillations result from an interaction between AOB-MCs and GCs. This conclusion is based on spatial analysis of LFP waveforms (**Fig. 5**) and previous work in slices (Jia et al., 1999). Notably, however, in the MOB these circuit elements were proposed to underlie the much faster gamma rhythm (Kersen et al., 2022, Li and Cleland, 2017, David et al., 2015, Fukunaga et al., 2014). This discrepancy may be reconciled by the fact that AOB and MOB neurons differ in intrinsic properties (Shpak et al., 2012, Zibman et al., 2011), connectivity (Larriva-Sahd, 2008), and the inputs they receive. All of these features (and others as well) can markedly affect oscillation frequencies (Li and Cleland, 2017, Kersen et al., 2022, Burton and Urban, 2021) and thus potentially account for the phenomenology of the oscillations observed here. Further experimental and modeling studies of the AOB network are required to pinpoint the mechanisms that give rise to AOB oscillations.

The potential role of active sampling behavior and its influence on sensory inputs is widely discussed in MOS contexts. There, active sampling behavior can modulate the activity of sensory neurons, and hence of downstream targets (Ackels et al., 2020, Jordan et al., 2018, Lefevre et al., 2016, Wachowiak, 2011, Verhagen et al., 2007, Kepecs et al., 2007). This similarity highlights another potential source of the oscillations, namely the vomeronasal pump itself. While there is evidence for intrinsic rhythmicity of the pump (Meredith, 1994, Meredith and O'Connell, 1979), it is not possible to determine whether it plays a role in the oscillations that we see here. One possibility is that more intense investigation can give rise to different pump dynamics, and hence change sensory neuron activity patterns, which in turn shape AOB input patterns. To reveal the effect, if any, of active sampling on these oscillations, it will be necessary to record them in awake behaving animals. Alternatively, VNO sampling may not be as amenable to controlled voluntary modulation as is sniffing, raising the idea that the AOB network evolved an intrinsic oscillatory mechanism serving a similar functional role (i.e., gating, binding, and multiplexing). Along the same lines, it is quite feasible that inputs from other brain regions can modify AOB neuron excitability and thus modulate the presence and expression of oscillations. This possibility can be investigated by enhancing, or diminishing, feedback inputs from other brain regions (Markopoulos et al., 2012, Cadiz-Moretti et al., 2014, Fan and Luo, 2009).

The physiological relevance of the oscillations

The existence and prevalence of the stimulus-induced theta oscillations beg the question whether they play a role in information processing. We strongly advocate the view that they are not an epiphenomenon, but rather reflect an important feature of AOB physiology. Below we propose several models, all of which are inspired by previous work in the MOS (Smear et al., 2011, Cury and Uchida, 2010, Chaput, 1986, Frederick et al., 2016, Osinski and Kay, 2016, Kay, 2015, Gschwend et al., 2012, Uchida et al., 2014, Fourcaud-Trocme et al., 2018, David et al., 2015, Cenier et al., 2009, Losacco et al., 2020, Jiang et al., 2017, Zelano et al., 2016, Schoppa, 2006, Burton and Urban, 2021), and other regions (Buzsáki, 2006).

One prominent aspect of the VNS and the AOB is its integrative structure. Without overlooking the important role of labeled line coding in the AOB (Ishii et al., 2017, Osakada et al., 2018, Ferrero et al., 2013), many natural stimuli are complex blends of molecules (Kahan and Ben-Shaul, 2016, Ben-Shaul et al., 2010, Hammen et al., 2014), and this implies that stimulus recognition may involve integration of information across channels (Kaur et al., 2014). Indeed, AOB circuitry itself already realizes substantial integration, as AOB-MCs often sample information from multiple glomeruli (Larriva-Sahd, 2008, Mohrhardt et al., 2018, Takami and Graziadei, 1991, Wagner et al., 2006). If distinct channels convey related information, there may be an advantage for these channels to be co-active. Thus, one simple hypothesis (**Fig. 8A**) is that the oscillations serve as a mechanism to constrain neuronal firing to limited temporal windows, in a manner that could activate downstream regions more efficiently. In this scenario, the oscillations serve a gating and amplification function: low neuronal activity levels will not give rise to oscillations, but once the activity is high enough, oscillations will appear, constrain spike timing to smaller windows, and thus result in more efficient information transfer. This scenario is strongly supported by the results shown in **Fig. 7B, F, G** and the analysis in **Fig. S10**. We stress that this model, as well as the others proposed below, rely on the observations that LFP oscillations are in phase throughout the extent of the AOB ECL (**Fig. S9**).

A more elaborate hypothesis suggests the existence of multiple ensembles, so that members of each are activated together. Under this scenario (**Fig. 8B**), neurons within an ensemble share a similar phase preference and are thus more likely to exert a synergistic effect on downstream targets. The notion that different units follow distinct phase preferences is supported by the analysis shown in **Fig. 7C**. However, unlike the MOS, where spike times of neurons "tile" the theta breathing cycle (Shusterman et al., 2011, Cury and Uchida, 2010), here most of the activity is concentrated within about a third of a period. Finally, the most elaborate scenario holds that phase distributions of units are stimulus-dependent (**Fig. 8C**). According to this model, each neuron can participate in different ensembles depending on the stimulus. Support for this idea comes from the analyses shown in **Fig. 7D, E**.

The two latter models may seem inconsistent with the idea, promoted also by us (Yoles-Frenkel et al., 2018) and others (Zibman et al., 2011), that the VNS is a slow and temporally imprecise system. However, there is no discrepancy between our previous conclusions and the present observations, since the synchronization proposed here involves joint activity of neurons rather than their locking to sensory stimulation on a trial-by-trial basis. Notably, while all the proposed models serve to enhance efficiency of downstream information transfer, the latter two also increase the coding capacity of the AOB network (via multiplexing).

Potential effects of coordinated activity on downstream processing stages

As we have shown above (**Fig. S10**), even a modest degree of phase-dependent firing can exert a profound effect on joint neuronal firing probability within a limited temporal window. The actual effect depends on the integrative properties of downstream processing stages, whose details are not known to us. This includes the extent of anatomical convergence, and the spatial and temporal synaptic integrative properties of neurons in these regions. Presently, our findings highlight and implicate a potential mechanism that cannot only gate, but can also bind and multiplex activity from distinct neuronal elements (**Fig. 8**). Understanding which, if any, of these mechanisms play a role in AOB information readout remains a central goal for future research.

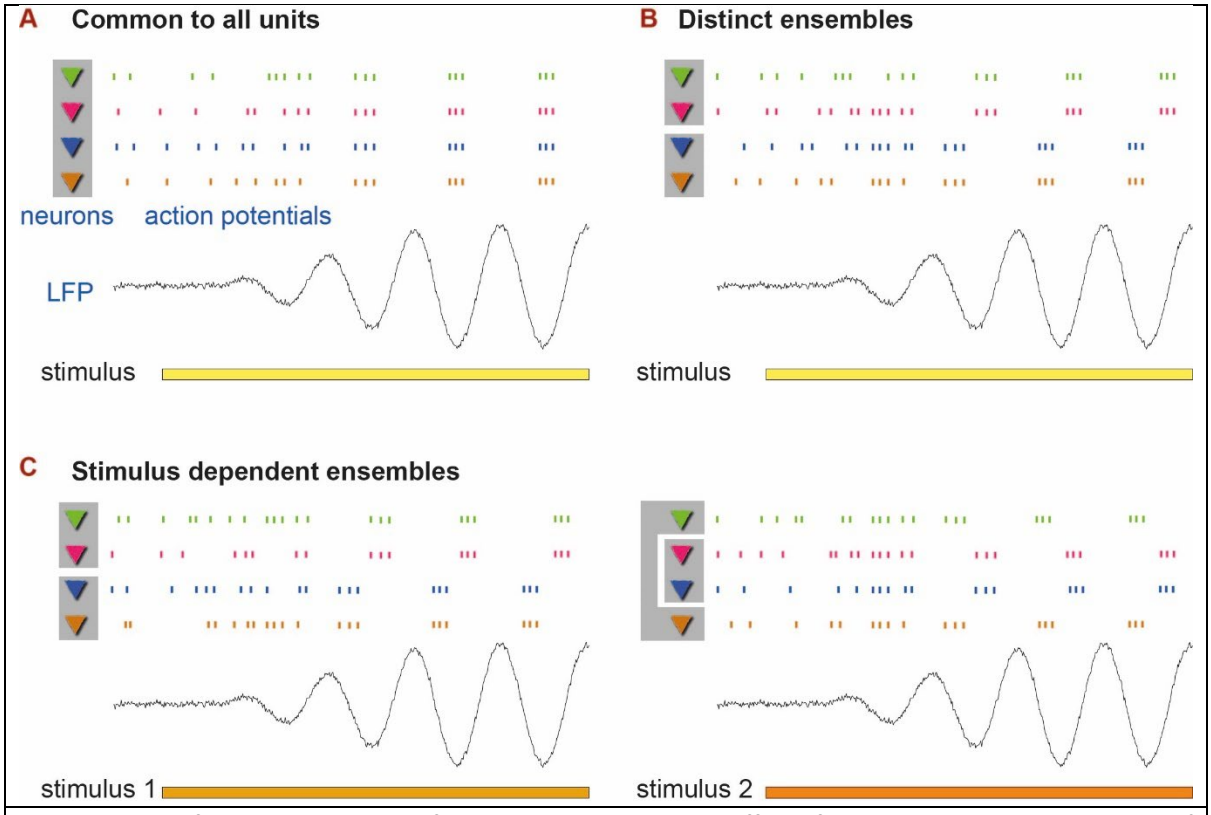

Fig. 8. Models of physiological roles of theta oscillations and the effect of phase concentration. Cartoons of three different scenarios for phase dependent spike timing. In each scenario, we show spike trains generated by 4 neurons, and a few periods from an LFP oscillation. Stimulus presentation is indicated by the colored bars at the bottom. Shaded regions behind neuron icons represent co-active ensembles. **A.** Uniform locking of spikes from all neurons regardless of the stimulus to a certain phase. In this scheme, oscillations can serve as a gating and amplification mechanism that does not distinguish between units or sensory stimuli. **B**. Locking of spikes, so that each unit has a preferred phase within the broad region of preference. In this scenario, there may be distinct ensembles that represent distinct stimuli. **C**. Stimulus and unit dependent phase locking. In this scheme, an elaboration of B, ensemble memberships may change as a function of the stimulus.

Materials and Methods

Subjects

For recordings, adult sexually male and female mice from the BALB/C and ICR strains were purchased from Envigo Laboratories (Israel). All experiments were performed in compliance with the Hebrew University Animal Care and Use Committee. A detailed description of the strains and sexes used in each session appears in **Table 1**.

Stimuli

Stimuli were collected from adult estrus and non-estrus sexually-naïve female mice of the BALB/C, C57BL/6 and ICR strains (Envigo Laboratories, Israel), as well as castrated, naïve, and sexually experienced male mice from the BALB/C and C57BL/6 and ICR strains. Some experiments also included a mixture of predator urine (purchased from PredatorPee, Maine, UAS) or a ringer's control stimulus. For mouse urine collection, mice were gently held over a plastic sheet until they urinated. The urine was transferred to a plastic tube with a micropipette and then flash-frozen in liquid nitrogen and subsequently stored at -80°C. Three of the sessions were previously analyzed in a different context and include urine, saliva, and vaginal secretion stimuli, as described in (Kahan and Ben-Shaul, 2016).

One session used urine stimuli with different pH values, and was previously included in (Cichy et al., 2015). See **Table 1** for a detailed description of the stimulus sets.

Experimental design

Experimental procedures were detailed in (Yoles-Frenkel et al., 2017), and are described briefly here, with the differences noted. Mice were anesthetized with 100mg/kg ketamine and 10mg/kg xylazine, a tracheotomy was performed with a polyethylene tube to allow breathing during flushing of the nasal cavity, and a cuff electrode was placed around the sympathetic nerve trunk with the carotid serving as a scaffold. Incisions were closed with Vetbond (3M) glue and the mouse was placed in a custom-built stereotaxic apparatus where anesthesia was maintained throughout the entire experiment with 0.5-1% isoflurane in oxygen. In parallel penetrations, a craniotomy was made immediately rostral to the rhinal sinus, the dura was removed around the penetration site, and electrodes were advanced into the AOB at an angle of ~30° with an electronic micromanipulator (MP-285; Sutter Instruments, Novato, CA). In perpendicular recordings, the craniotomy was made caudal to the rhinal sulcus and the electrodes advanced approximately at 60°. All recordings were made with 32 channel probes with either 8 channels on each of 4 shanks (NeuroNexus Technologies, Ann Arbor, Michigan) or 16 channels on each of 2 probes (see **Table 1**). Due to an oversight, some of the sessions include LFP recordings from only 16 channels (rather than 32, see **Table 1**). Unless indicated otherwise, data from these sessions are also included in our analysis, as the 16 channels (spanning the superficial half of the probe) were sufficient to derive the TMS (see **Fig. S2**). Before recordings, electrodes were dipped in fluorescent dye (DiI, Invitrogen, Carlsbad, CA) to allow subsequent confirmation of electrode placement within the AOB ECL, which contains the mitral-tufted cells (Larriva-Sahd, 2008). In each session, stimuli were typically presented 5 times in a pseudorandom order. In each presentation, 2 µl of stimulus was applied directly into the nostril. After a delay of 20 s, a square-wave stimulation train (duration: 1.6 s, current: ±120 µA, frequency: 30 Hz), was delivered through the sympathetic nerve cuff electrode to induce VNO pumping and stimulus entry to the VNO lumen. Following a second delay of 40 s, the nasal cavity and VNO were flushed with 1-2ml of ringer's solution which flowed from the nostril, into the nasal cavity, and sucked out from the nasopalatine duct via a solenoid-controlled suction tube. The cleansing procedure lasted 50 s and included sympathetic trunk stimulation to facilitate stimulus elimination from the VNO lumen.

Electrophysiology

Neuronal data was recorded using an RZ2 processor, PZ2 preamplifier, and two RA16CH head-stage amplifiers (TDT, Alachua, FL). LFP data was collected at 508.63 Hz and band-pass filtered at 0.5 to 300 Hz ("EEG" setting on the TDT system). As described below, a notch filter was applied to remove 50Hz line noise. Single-unit and multi-unit activity were sampled at 24414 Hz, band-pass filtered (300-5000 Hz) and custom MATLAB (Mathworks, Natick, MA) programs were used to extract spike waveforms. Spikes were sorted automatically according to their projections on two principal components on 8 channels of each shank using KlustaKwik (Csicsvari et al., 2003, Hazan et al., 2006) and then manually verified and adjusted using the Klusters program (Hazan et al., 2006). Spike clusters were evaluated by consideration of their spike shapes, projections on principal component space (calculated for each session individually) and autocorrelation functions. A spike cluster was defined as a single unit if it had a distinct spike shape and was fully separated from both the origin (noise) and other clusters along at least one principal component projection, and if its inter-spike interval histogram demonstrated a clear trough around time 0 (of at least 10 ms). Clusters comprising more than one single-unit were designated as multi-units. Thus, using the present definitions, multi-units could represent the activity of as few as two units, or more. In most of the analyses here we used single-unit data. When using multi-unit data, this is indicated explicitly. We note that our multi-units are not equivalent to what is

commonly referred to as multi-unit activity and which includes above threshold signals in each of the electrodes. The latter are not included in our analyses. As a further criterion of our single-unit data, we examined all spike shapes by calculating the shape symmetry. The symmetry is a good measure for accidental noise that was misclassified, which yields high symmetries. Using a graphical representation of all spike shapes, we examined the entire data set for such noise like spikes and these were excluded from all analysis.

Data analysis

Generally, all analyses were conducted in MATLAB, using built-in MATLAB functions when available, or custom code as needed. Initial, exploratory data analysis was performed using a custom-written data browser that allowed viewing all LFP and electrode data, superposed with trial events and manual oscillatory event definition. The interface was instrumental for revealing the oscillatory episodes that form the basis of this study. Using this browser, we viewed the entire data set comprising 34 recording sessions and eventually converged upon the following analysis procedure, comprising three major conceptual stages.

Stage 1. Manual definition of oscillatory events for each session. For each session, we typically defined several events (See **Fig. S1**) that were used as seeds to derive the LFP template using custom code. For each of these events, we calculate the mean LFP envelope, for each of the channels, across all samples. **Fig. 2D** shows these envelopes for each of the defined segments. The template itself (e.g., **Fig. 2E**) is simply the mean of these events' envelopes. During this stage, we sometimes also identified and defined broken (and hence noisy) channels, which were excluded from TMS calculation. The template is then saved in a data file and used in subsequent processing stages.

Stage 2. Analysis of the data in each session using a wrapper function. Given a data session as input, the function loads the LFP data, spike data (including both spike times and definitions of unit classifications, i.e., single vs. multi units), event data (e.g., trial events such as stimulus presentation and stimulation), the envelope template (from stage 1), and electrode configurations. Using this information, the function conducts multiple steps of analysis which are saved as MATLAB figures and a data structure (for each session).

Stage 3. Finally, we run several scripts that load the results data from multiple sessions, as generated by the previous stage, and conduct global analyses on this combined data. These scripts serve various purposes such as analysis of basic episode features, spatial distributions of the template, relationships between LFP and single-unit data, phase analyses and so on.

All data figures in this manuscript are generated by MATLAB, exported to adobe illustrator where they were resized or altered graphically (colors, line widths, etc.) for a clearer presentation. *All the functions and scripts, and data and figure files generated by these functions are available upon request.*

Below is a description of the analysis steps included within stage 2, as applied to each of the sessions. Many of the calculations performed by the analyses scripts in stage 3 employ the same algorithms as in stage 2, and are described in the corresponding sections in the manuscript.

Analysis procedure per session

1. Basic LFP processing. We load LFP data, apply a notch filter (to remove the 50Hz line noise) using the MATLAB *filfilt* function. The filter is defined with the *designfilt* MATLAB function using the following parameters: type: bandstopiir, FilterOrder: 20, HalfPowerFrequency1: 49,

HalfPowerFrequency2: 51, SampleRate: 508.63. The LFP envelope is derived with the MATLAB *envelope* function with the *rms* option, and a window of 0.1 seconds.

2. Derive the LFP template match signal (TMS), by calculating the linear correlation (using the MATLAB *corr* function) between the template (derived as described above), and the LFP envelope at each point in time, across the active channels. The signal is then smoothed with a 0.5 s Gaussian window (using the MATLAB *smoothdata* function), rectified (so that negative values become 0), and raised to the 10th power to enhance contrast. As described in the main text, the template is the mean LFP envelope across all channels, in manually defined events. When averaging across manually defined events, we first derive the mean envelope associated with each event, and then average across events (so that each event has the same contribution, regardless of its duration).

3. Detect candidate episodes. We apply a threshold on the LFP template signal. We used the mean signal due to its simplicity, and the fact that it was typically lower than other thresholding methods that we tested. A lower threshold implies more detected episodes and hence larger samples for statistical analyses. After setting a threshold, we obtain a binary template signal. All such detected sections that are at least 1 s long are considered as potential episodes.

4. Ridge extraction and phase derivation. Rationale: The spectro-temporal analyses in this work were based on the wavelet synchro-squeezed transform (WSST) (Daubechies et al., 2011, Thakur et al., 2013). We chose this approach because it includes a "reassignment" step that enhances temporal and spectral estimates by compensating for spreading effects of the base wavelet, and because it facilitates ridge extraction using the built-in MATLAB functions. A ridge is a sequence of (typically smoothly varying) frequencies and their amplitudes in time, and ridges are thus particularly suitable for analyzing signals that contain a significant chirp-like component, like the oscillations analyzed here. Multiple ridges can be extracted, with the first ridge being the maximum energy time-frequency ridge, and subsequent ridges showing decreasing energies. The inverse WSST (iWSST) reconstructs the original signal in the time domain from the transform generated by the WSST. It is also possible to reconstruct the original signal using one or more ridges. If a ridge provides a good description of the original signal, then reconstruction based on it will yield a result similar to the original signal. In our analysis, we focused on episodes for which a single ridge can provide a good reconstruction (reconstruction score, defined as the correlation coefficient between the original signal and its reconstruction). Analysis based on ridges rather than on a narrow frequency band is crucial because any given frequency band might either miss oscillatory components, or contain non-oscillatory components. In addition, instantaneous phases of signals that contain multiple frequency bands are often ambiguous, whereas signals that are composed of a single ridge contain a single frequency at each point in time and thus are associated with an unambiguous phase.

Practically, we consider the channel with the highest LFP energy and then apply the wavelet synchro-squeezed transform on this signal (using the MATLAB *wsst* function). Focusing on one channel is warranted given the high correlation at 0 lag among all channels in a given episode, as calculated by the cross covariance (MATLAB *xcov* function) of all channels (**Fig. S9**). We then remove all frequency contributions above 40Hz (which are substantially above our range of interest), and then extract the first 3 ridges using the *wsstridge* MATLAB function, using a *penalty* value of 5. Higher *penalty* values favor ridges without abrupt changes in the frequency domain. We then define the mean frequency of each ridge as the weighted mean frequency across all bins, where the weighting is given by the amplitude (the absolute value of the WSST in the corresponding bin). Next, we reconstruct the original episode using the inverse wavelet synchrosqueezed transform (*iwsst* MATLAB function). Episodes are

reconstructed using the first ridge (and for demonstration, as in **Fig. S5**, with the all the first three ridges). We then calculate the correlation coefficient between the original signal and the reconstruction and derive the instantaneous phase of the reconstructed signal using the first ridge. The instantaneous phase is obtained by taking the angle (MATLAB *angle* function) of the Hilbert transform (MATLAB *hilbert* function). At this stage, we have a set of episodes, with associated phases, reconstruction scores, and other measures such as the mean frequency (as described above), mean template match and mean envelope energy. The relationships between these various measures are shown in **Fig. S6**.

5. Selection of episodes for further analysis. For further analysis, we only select episodes that pass two criteria. First, the correlation coefficient between the first ridge reconstruction and the actual data is larger than 0.5. A higher correlation implies that the single ridge provides a good description of the original signal. Second, the mean frequency is within the broad theta range: 2-14 Hz. This range was selected after we conducted extensive manual inspection of oscillatory events and concluded that virtually all such oscillations are within the range. The mean frequency is the mean across all time points, with the frequency in each time point weighted by the amplitude of the ridge during that sample. Next, we manually exclude episodes whose high correlation score is not due to a good reconstruction of the theta mode of the episode ("false positives"), and identify episodes that include obvious oscillatory modes, are noise free, and complete (i.e., that the entire oscillatory episode appears uninterrupted by noise) ("complete" episodes). The rest, which are the majority of episodes are designated as good episodes. Unless indicated otherwise, we used good and complete episodes in our further analyses. Complete episodes are mainly used for in-depth analyses such as CSD analyses. When a distinction is made between good and complete episodes, this is indicated in the text.

6. Current source density was calculated for each of the complete episodes as the second derivative of the LFP signal along the probes within a given shank (Mitzdorf, 1985). The CSD as a function of time is smoothed using the MATLAB *smoothdata* function with a gaussian window and a smoothing window of 20 ms.

7. Analysis of the LFP and unit signals with respect to sensory events. To study the relationship between the TMS and the sensory events, we considered all stimulus presentation epochs. The stimulus presentation epoch begins with stimulus *application* to the nostril, and ends 40 seconds after the electrical nerve *stimulation*, for a total period of 60 seconds. Some of our analysis and displays include margins of 5 s at the beginning and ends of this epoch, for a total duration of 70 s per stimulus. For each of these epochs we derived the LFP template match signal, the binary template match signal (as defined above) and the spiking rates of each of the units (spiking rates were calculated in 0.2 s windows and then smoothed with the MATLAB *smoothdata* function, using a 1s *gaussian* window). With this approach we could retrieve the continuous TMS associated with individual trials, the mean template match signal associated with all trials of a given stimulus (within a recording session), and the number of samples in which the template match signal was above threshold. In addition, we derived the LFP envelope (that is the LFP rms signal itself rather than the TMS) associated with each stimulus. The LFP envelope was evaluated during samples in which the binary template signal was above threshold. Thus, the accuracy of the envelope estimate depends on the number of samples during which there was above threshold match with the template. In some cases, there were no such samples for a given stimulus and session.

8. To correlate firing rates of individual units (or all units together) with the LFP template signal, we first resampled the spiking rates by binning spike counts into bins that match the LFP sampling rate, and then smoothed them using a 5 s gaussian window (using the MATLAB *smoothdata* function). The relatively long window was chosen to reduce noise in the estimate of the firing rate and thus in the correlation between the spiking and LFP signals. The correlations between spike and LFP envelope signals were calculated using the MATLAB *xcov* function, with scaling set to *normalized*.

9. Spike time phase analysis. Spiking phases were only measured during oscillatory episodes (good or complete episodes as defined above). Recall that these are data episodes for which the first ridge mean frequency is within the theta range and that it yields a reconstructed signal with a correlation of at least 0.5 with the original full signal. Each sample in each episode is associated with an instantaneous phase (see above). Then, for each of the units, spikes that occurred within that episode are found, and for each we find the nearest LFP sample. In this way, a phase is associated with each of the spikes of each of the units within each of the different stimuli (that were presented during that session). Importantly, during this process we also derive shuffled phase distributions. These are obtained by randomly reordering the phases associated with each episode (using the MATLAB *randperm* function). The random permutation is applied independently to each unit within each of the episodes (and hence stimuli). This last detail is significant as it abolishes phase dependencies of simultaneously recorded units. For both real and shuffled data, composite spike phase distributions of each unit are obtained by combining phase distributions across all stimuli. For statistical analyses of the phases, we used the MATLAB circ_stat toolbox (Berens, 2009), and specifically the following functions: *circ_otest* for uniformity of data, *circ_mean* for the circular mean. For pairwise comparisons of phase distributions, we use the *circ_cmtest* function, which is a non-parametric test that compares medians of two samples. For all our analyses, we only evaluated phase distributions (whether for individual neurons or for specific unit-stimulus combinations) if the number of spikes within the samples was at least 50.

<u>Analysis procedures across sessions</u>

To statistically compare stimulus triggered averaged TMS (staTMS) across different stimuli, (as described in the text in relation to **Fig. 3D** and **Fig. S3 C**) we combined the staTMS (across all trials for each stimulus) across all sessions. Thus, the number of data points associated with each stimulus is the number of sessions multiplied by the number of samples in each data cut. Given our LFP sampling rate of 508.63 Hz a data segment of 70 s (beginning 5 s before stimulus presentation and ending 65 after it), this yields 35605 samples. Each sample is associated with one type of stimulus, and then a non-parametric ANOVA (MATLAB *kruskalwallis* function) is used to test the null hypothesis of equal medians for all stimuli.

To compare the envelope shape associated with different stimuli, we calculated the correlation coefficient between the mean LFP envelopes associated with each of the stimuli. To reveal if the degree of correlation was a trivial outcome of stimulus magnitude, we also calculated the summed envelope (across all channels) for each stimulus and then calculated the pairwise energy differences across all stimulus pairs. This analysis is described and further explained in **Fig. S4**. This allowed us to evaluate if template shape similarities were due to intensity similarities.

In several analyses (e.g., phase analyses), we associated oscillatory episodes with specific stimuli. An episode was associated with a stimulus if, and only if, it is was entirely included within a given stimulus epoch (as defined above).

To conduct pairwise comparisons of phase distributions between all pairs of neurons, we considered each pair of units. We conducted a comparison if, and only if, at least one of the two units under comparison, or their shuffled distributions, had a non-uniform phase distribution ($p < 0.05$ as determined using the *circ_otest*). We used this procedure because we reasoned that there is no meaning to comparing median phases of two distributions of which neither deviates from uniformity. We also considered phases of the shuffled distributions in order to make the comparison between real and shuffled distributions more balanced. If inclusion based on non-uniformity is only based on the real distribution, this presents a bias against the shuffled distributions leading to even greater differences than those observed here between the real and shuffled distributions. The same procedure was applied for comparison of phase distributions associated with pairs of stimuli for particular neurons. Specifically, we only compared pairs of phase distributions if at least one of the members (in either the real or shuffled data) significantly deviated from uniformity ($p < 0.05$ as determined using the *circ_otest*). We stress that our results remain entirely valid (with unequivocal differences between real and shuffled data) using other criteria for inclusion in comparisons (for example, when considering all pairs of distribution samples regardless of deviation from uniformity, or conversely, when considering only pairs in which both samples significantly deviate from uniformity).

Calculation of the probability of observing a certain number of action potentials within a window (**Fig. S10**): We used the MATLAB *binocdf* function, to calculate the upper tail of the cumulative probability to obtain x or more spikes from a population of N neurons with a certain firing rate (f). More specifically (if f is not too large), a Poisson neuron (i.e., fixed firing probability at each point in time) with a baseline rate of f Hz has a firing probability of f/1000 within a 1 ms window. Thus, the mean number of spikes emitted by n neurons within a temporal window of s ms is simply f•s•n. To quantify the effect of phase dependent firing, we compare the result when f is multiplied by various factors (1.1, 1.5, and 2).

All the raw data, processed data, and codes will be provided by the authors upon request.

Session	EXP	Sex	Strain	PROBE	ID	Δ SITE	Δ SHANK	SA	CHANS	OR	EXP
13oct13_2	A	male	BALB/C	4x8	46A2	100	200	177	16	PAR	AK
28oct13_1	A	male	BALB/C	4x8	46A5	100	200	177	16	PAR	AK
30oct13_1	A	male	BALB/C	4x8	46A5	100	200	177	16	PAR	AK
12dec13_1	B	male	BALB/C	4x8	46A6	100	200	177	16	PAR	AK
20oct14_1	C	male	BALB/C	4x8	45FA	100	200	177	16	PAR	AK
06jan16_1	D1	male	BALB/C	4x8	4601	100	200	177	16	PAR	AK
07jan16_1	D1	male	BALB/C	4x8	4601	100	200	177	16	PAR	AK
07jan16_2	D1	male	BALB/C	4x8	4601	100	200	177	16	PAR	AK
11jan16_1	D1	male	BALB/C	4x8	4601	100	200	177	16	PAR	AK
13jan16_1	D1	male	BALB/C	4x8	4601	100	200	177	16	PAR	AK
13jan16_4	D1	male	BALB/C	4x8	4601	100	200	177	16	PAR	AK
28jan16_1	D2	male	BALB/C	4x8	46A6	100	200	177	32	PAR	AK
03feb16_1	D2	male	BALB/C	4x8	4601	100	200	177	32	PAR	AK
03feb16_4	D2	male	BALB/C	4x8	4601	100	200	177	32	PAR	AK
07feb16_1	D2	male	BALB/C	4x8	4601	100	200	177	32	PAR	AK

07feb16_4	D2	male	BALB/C	4x8	4601	100	200	177	32	PAR	AK
26feb18_1	E	male	BALB/C	2x16	4D3C	50	500	177	32	PERP	OC+SM
26feb18_2	E	male	BALB/C	2x16	4D3C	50	500	177	32	PERP	OC+SM
04mar18_1	E	male	BALB/C	2x16	4D3C	50	500	177	32	PERP	OC+SM
05mar18_1	E	female	BALB/C	2x16	4D3C	50	500	177	32	PERP	OC+SM
07mar18_1	E	male	BALB/C	2x16	4D3C	50	500	177	32	PERP	OC+SM
07mar18_2	E	male	BALB/C	2x16	4D3C	50	500	177	32	PERP	OC+SM
08mar18_2	E	male	BALB/C	2x16	4D3C	50	500	177	32	PERP	OC+SM
13mar18_1	E	female	BALB/C	2x16	4D3C	50	500	177	32	PERP	OC+SM
27jun18_1	F	female	ICR	2x16	4D3C	50	500	177	32	PERP	OC
31jul18_1	F	female	ICR	2x16	4D3C	50	500	177	32	PERP	OC
01aug18_1	F	female	ICR	2x16	4D3C	50	500	177	32	PERP	OC
18feb19_1	G	female	ICR	4x8	4AC3	50	200	413	32	PAR	OC
18feb19_2	G	female	ICR	4x8	4AC3	50	200	413	32	PAR	OC
05mar19_1	G	female	ICR	4x8	4AC4	50	200	413	32	PAR	OC
05mar19_2	G	female	ICR	4x8	4AC4	50	200	413	32	PAR	OC
07may19_1	G	female	ICR	4x8	4AC4	50	200	413	32	PAR	OC
07may19_2	G	female	ICR	4x8	4AC4	50	200	413	32	PAR	OC
16may19_1	G	female	ICR	4x8	4AC4	50	200	413	32	PAR	OC

Table 1: Details of the sessions used in this manuscript. The letters correspond to the experiment types indicated in the table.

A. Urine, saliva, and vaginal secretions, from estrus and non-estrus female mice, from the BALB/C and C57BL/6 strains. See further details in (Kahan and Ben-Shaul, 2016).
B: Urine from estrus and non-estrus female mice from the BALB/C strain at 1, 10 and 100F solution.
C: Male urine, Female urine at various pH values (5-7). See (Cichy et al., 2015).
D1, D2: Mixtures of male, female, and predator stimuli each at 1:100, 1:30, and 1:10 dilutions in Ringer's solution. Male and female mixtures included stimuli from the BALB/C and C57BL/6 strains. See (Yoles-Frenkel et al., 2018).
E: BALB/C female and male urine, predator urine mix, and ringer's solution. In these experiments, we did not perform a tracheotomy, since we wanted to maintain airflow in the nasal cavity during breathing. Because of this, we could not flush the nasal cavity with solution, and thus these experiments only contain a small number of trial repeats.
F: Undiluted urine mixes from castrated, dominant and naïve male mice. Each mix contains urine from the ICR, BALB/C and C57BL/6 strains. A mix of estrus and non-estrus female urine, predator urine mix, and ringer's solution.
G: Undiluted urine from naïve, dominant, and castrated male mice from the BALB/C, C57BL/6, and ICR strains (9 different stimuli), as well as urine mixes from estrus and non-estrus female mice, and a ringer's control stimulus.

Session: date and session number within date. Unique experiment ID, EXP: shorthand for type of experiment, SEX: sex of the subject mouse, STR: strain of subject mouse, PROBE: number of shanks x number of sites per shank in recording probe, ID: probe ID in the NeuroNexus catalogue, Δ SITE: vertical distance between sites on the same shank (μm). Δ SHANK: distance between shanks on the probe (μm). SA: site area (μm^2), CHANS: number of active LFP channels, OR: probe orientation. PAR: parallel to the AOB-ECL, PERP: perpendicular to the AOB-ECL. EXP: initials of lead experimenter.

Extended data

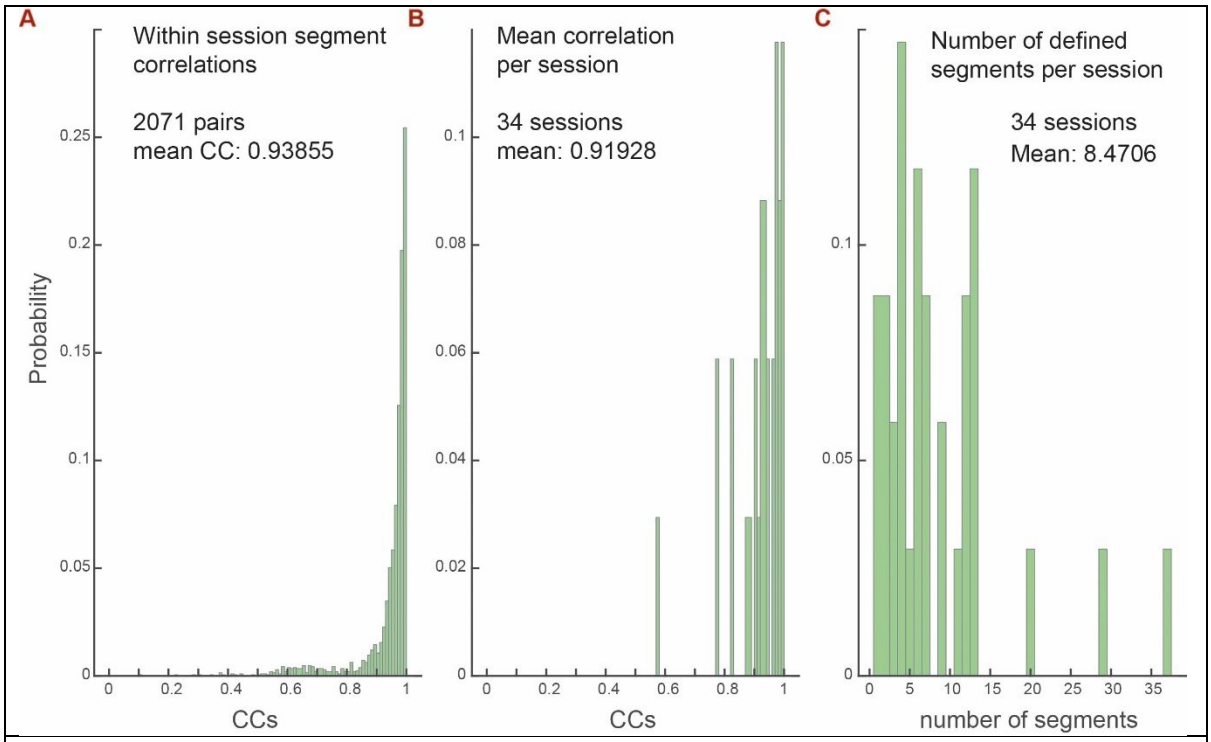

Fig. S1. Features of manually defined events ("seed" events). A. Distribution of cross correlation coefficients among all manually defined events within a session, pooled over all sessions. **B.** Distribution of the mean cross correlations among events, for each session. **C**. Distribution of the number of manually defined events per session.

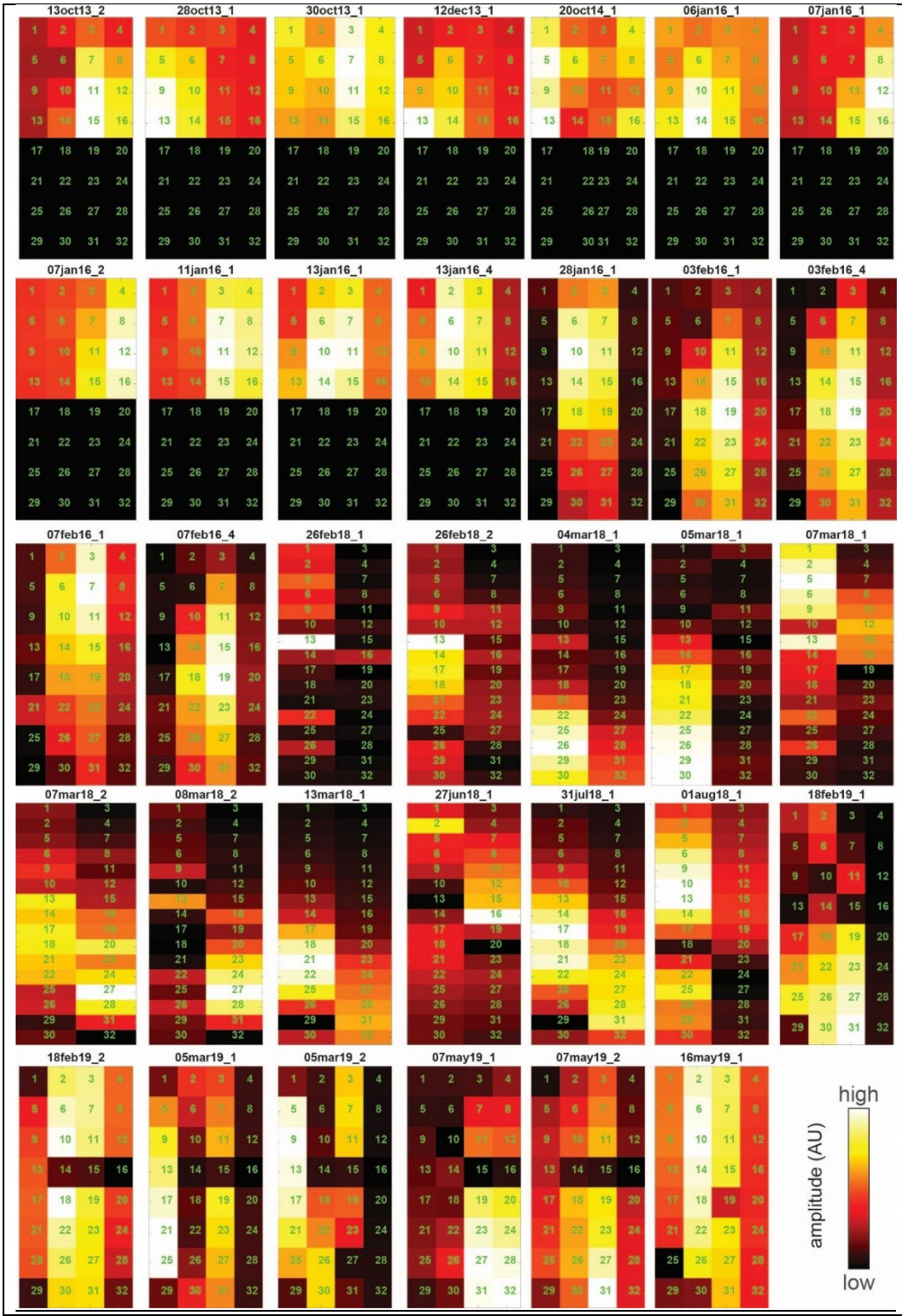

Fig. S2. Templates for each of the sessions in the database. Note that the first 11 recordings only include 16 channels. Note also that some recordings contain non-functional recording sites. (i.e., 14-16) in some of the recordings in the lowest row. These broken channels were excluded for template calculation.

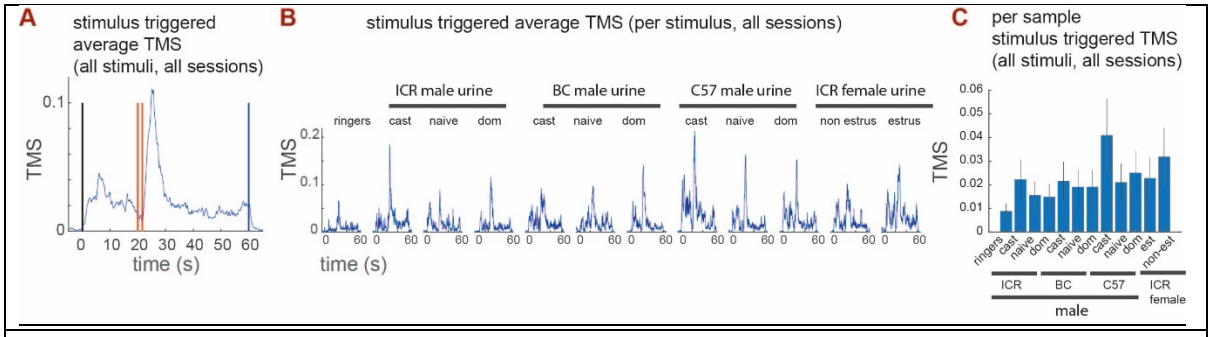

Fig. S3. The mean TMS, around all stimulus presentation times, in one type of experiment. Like Fig. 2 panels C-E, but for a different stimulus set (exp G, **Table 1**). **A.** Stimulus triggered average TMS (staTMS), around all stimulus presentation times, in one type of experiment. **B.** Average TMS for each stimulus separately. **C.** The mean template signal (directly proportional to areas in B) and the standard error across all presentations of each of the stimuli. See Table 1 for details on the stimuli used. Note that different stimuli elicit different TMS profiles, and that the control stimulus (ringers) induces the weakest response.

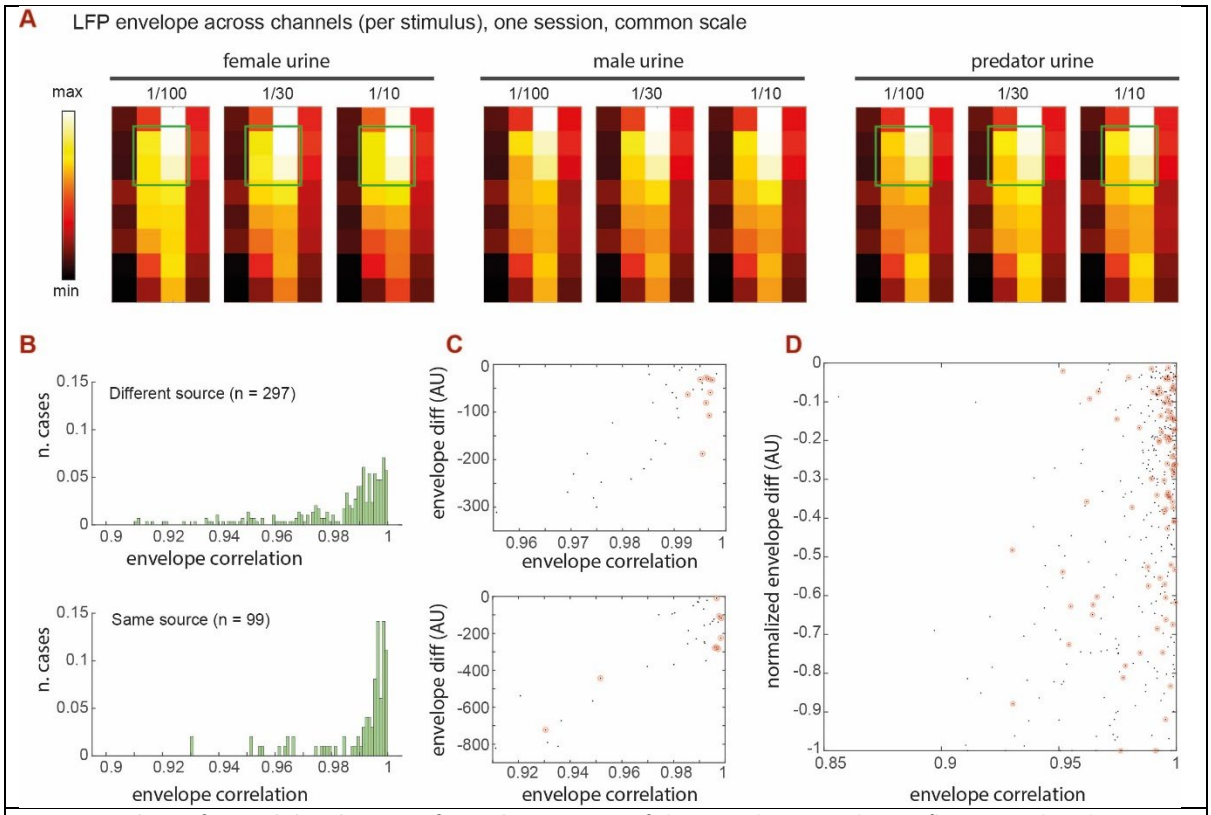

Fig. S4. Analysis of spatial distributions of templates. To test if the spatial LFP envelope reflects stimulus identity, we focused on a subset of sessions (n = 11) that included 3 stimuli, each at 3 different dilutions (Stimulus set D, **Table 1**). An example of envelopes during one such session is shown in **A**. Each envelope is normalized to its maximal value to highlight the similarity among them. While the similarity is obvious, it appears that envelope distributions associated with stimuli from the same source (e.g., two female stimuli at different dilutions) are even more similar to each other than are those from different stimuli. For example, compare the area highlighted by the green rectangles for female vs. predator stimuli. To quantify this notion, we measured the correlation between LFP envelope distribution across all channels, for each stimulus pair. We then compared the correlation coefficients for all pairs of same-source (n = 99), and different-source (n = 297), stimuli. **B** shows that although correlation values are very high for both groups, they are higher for stimulus pairs from the same source (means, different sources: 0.98, same sources: 0.99, medians, different sources 0.990 same sources: 0.996), and significantly different ($p = 1.09 \bullet 10^{-5}$, Kruskal Wallis test).

A high correlation among templates will also arise from the fact that typically only a subset of channels has substantial LFP energies (with others being close to 0). Thus, one potential caveat with our conclusion is that similarity might be a trivial result of similar amplitudes. In other words, if a given source elicits higher amplitude envelopes, then this will also give rise to higher correlations among them. If this is the case, one would expect a positive correlation between similarity in amplitude (calculated as the negative of the template sum difference) and shape similarity. Plotting

these two measures separately for each session, we observe that for most sessions there is indeed a positive correlation **C** shows two examples of sessions with high correlation. However, these examples also suggest that even for a given level of template sum differences, pairs of like stimuli envelopes (red-circled dots) are more similar than distinct stimulus envelopes (black dots without a circle). To examine this across the entire data set, we normalized the distances among envelopes (that is, distances were divided by the maximal distance among template envelopes within each session), and plotted all on the same panel (**D**). This representation again strengthens the notion that similar stimuli elicit a similar pattern of LFP envelope patterns. Specifically, when we compare the pairwise shape difference distributions separately for cases with high and low envelope similarity (distance smaller or larger than 0.4), the distributions of same and different source pairs are statistically distinct (p-value for distances smaller than 0.4: 0.00042189, N = 215, p-values for distances larger than 0.4: 0.038959, N = 181, Kruskal Wallis test).

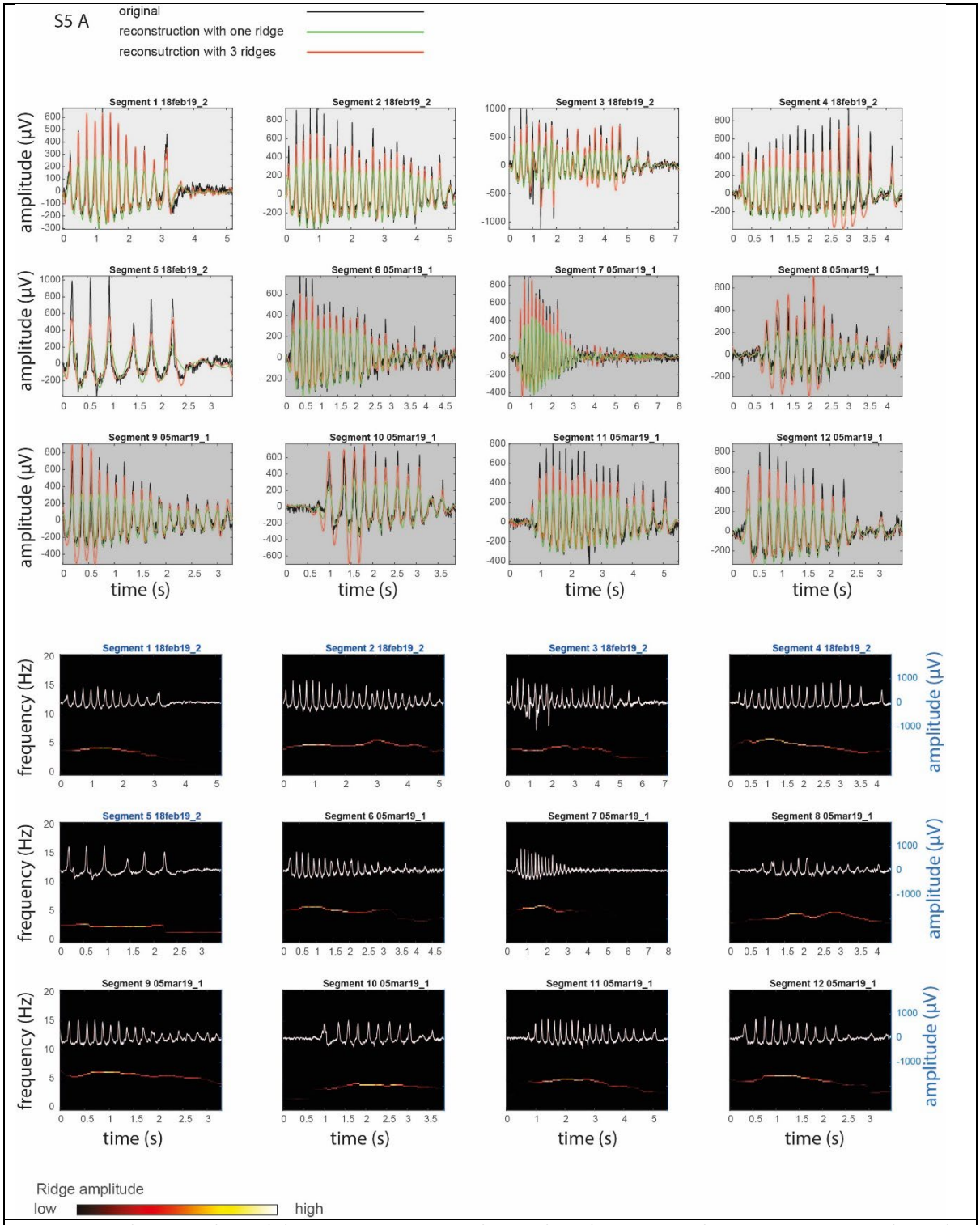

Fig. S5. Complete episodes and their reconstructions. Each episode is shown twice. The top representation shows the original episode (black), and its reconstruction using one (green), or all 3 ridges (red). The bottom representation shows the original episode (µV scale on the right) and the first ridge time frequency decomposition as a heat map. This is one of 8 figures which together show all complete episodes. The session from which the episodes is derived in shown above each panel (shown is one panel of eight).

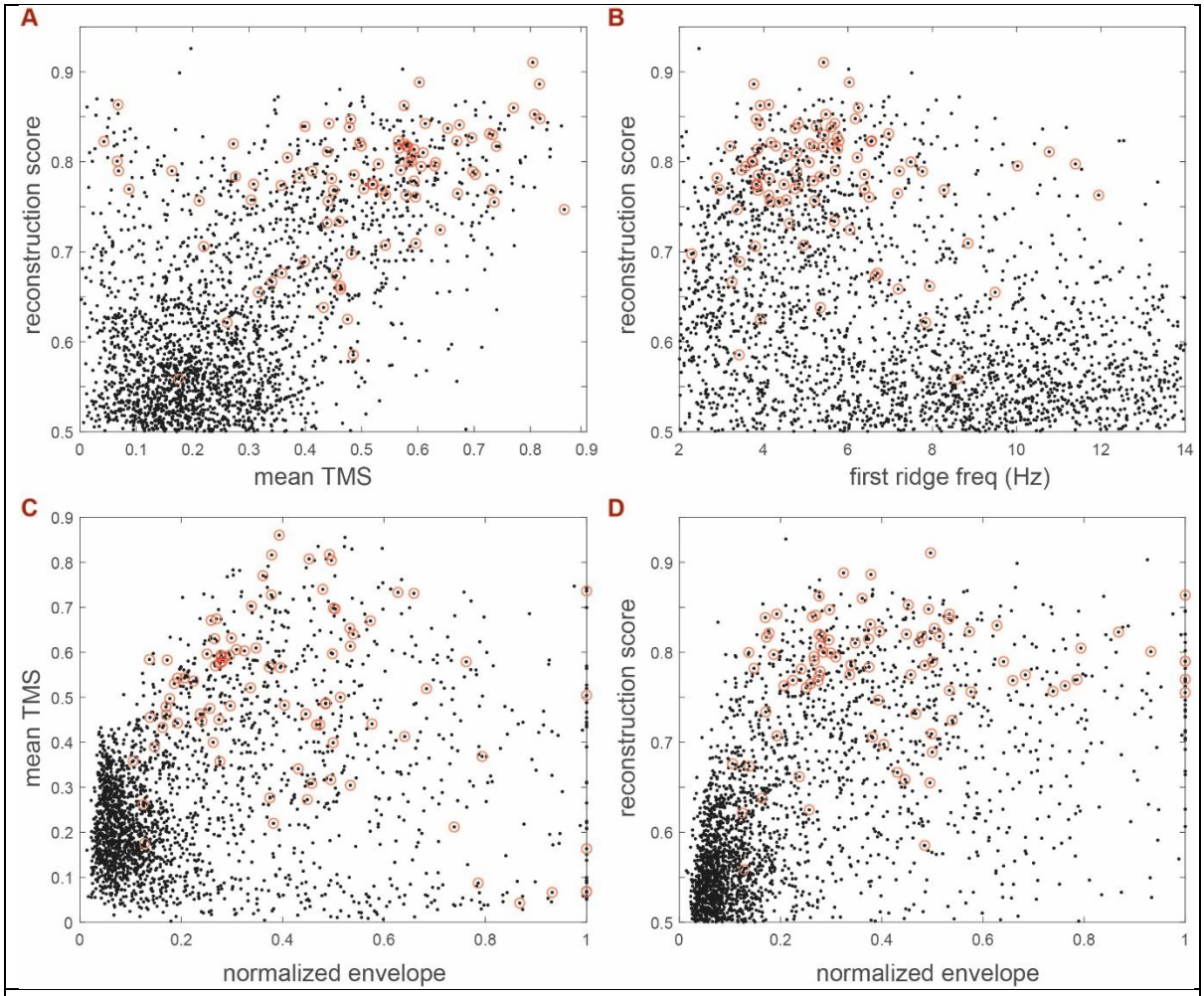

Fig. S6. General episode features. A. Reconstruction score (correlation coefficient between original signal and reconstruction with the first ridge) vs. mean TMS (across the entire episode). **B.** Reconstruction score vs. the mean first ridge frequency. **C**. Mean TMS vs. normalized envelope amplitude (envelope within each session was normalized by the envelope of the episode with the largest envelope). **D**. Reconstruction score as a function of normalized envelope. In all panels, black dots represent all episodes, and black dots with red circles correspond to *complete* episodes. Note the correlation between mean template match and a good reconstruction score, and the concentration of first ridge frequencies in the ~5Hz for the complete episodes.

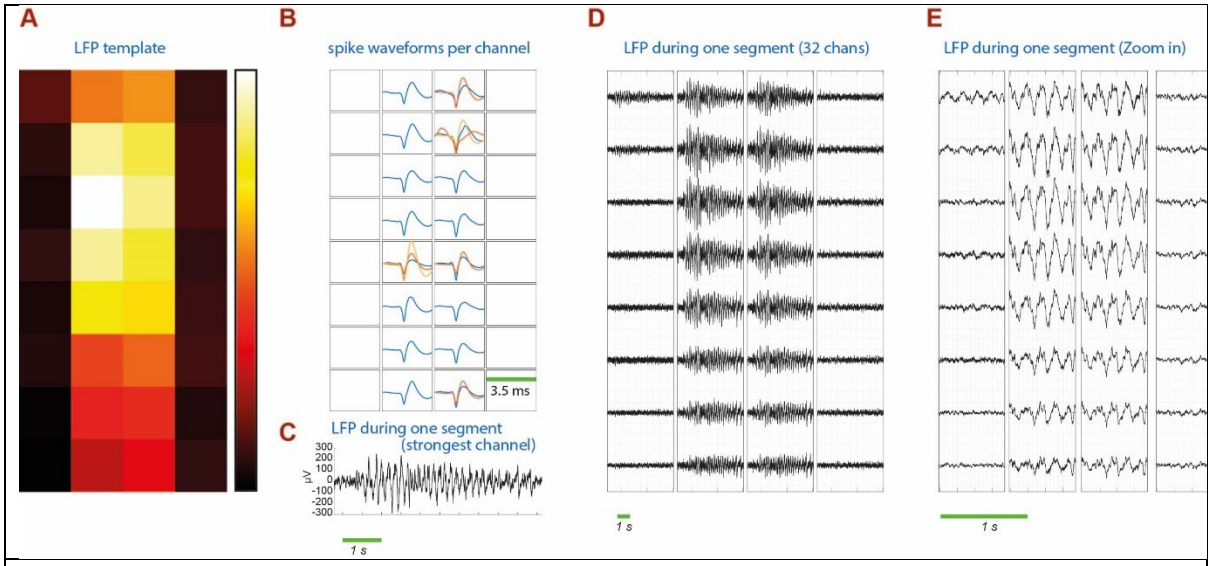

Fig. S7. Evidence for localization of oscillations within the AOB ECL. Like Fig. 5 panels A-F, but for another session. **A.** Spatial spread of LFP energies in one of the sessions. **B**. Spike waveforms in the sites shown in A. Each square shows the spike waveforms recorded in that channel. Both single unit and multi-unit activity waveforms are shown. **C.** Recording from one channel during an oscillatory episode. Shown is the channel with the maximal amplitude. **D.** LFP oscillations in the same episode shown in C, across all channels, plotted according to spatial position. **E.** Magnified temporal view of D, highlighting the phase similarity across all channels.

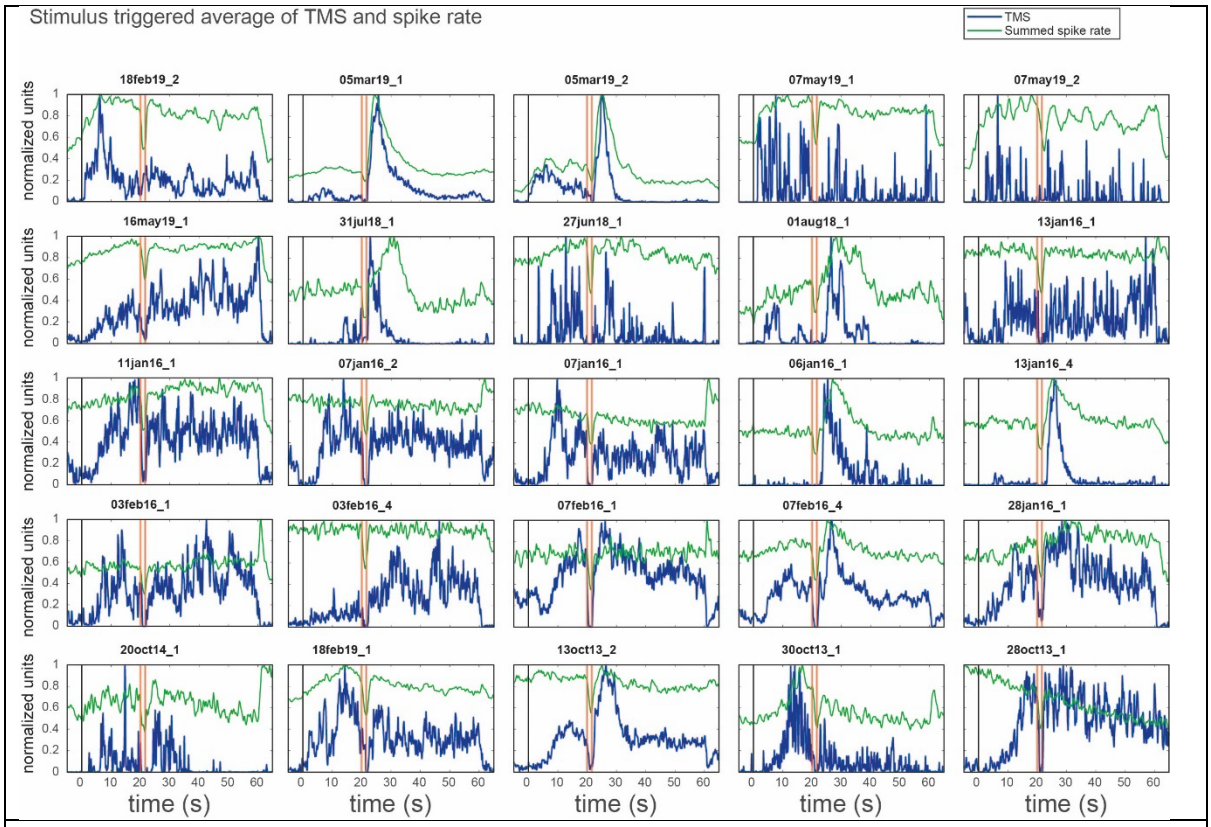

Fig. S8. Relationship between the TMS and summed single unit activity, across stimulus presentations. Same conventions as **Fig. 6D**, but with more sessions included. Stimulus triggered averages of both values were calculated across all stimuli. Green and blue traces correspond to the spike signal, and the TMS, respectively. Note that the TMS generally follows the stimulation time course more closely and is more localized in time than the spike signal.

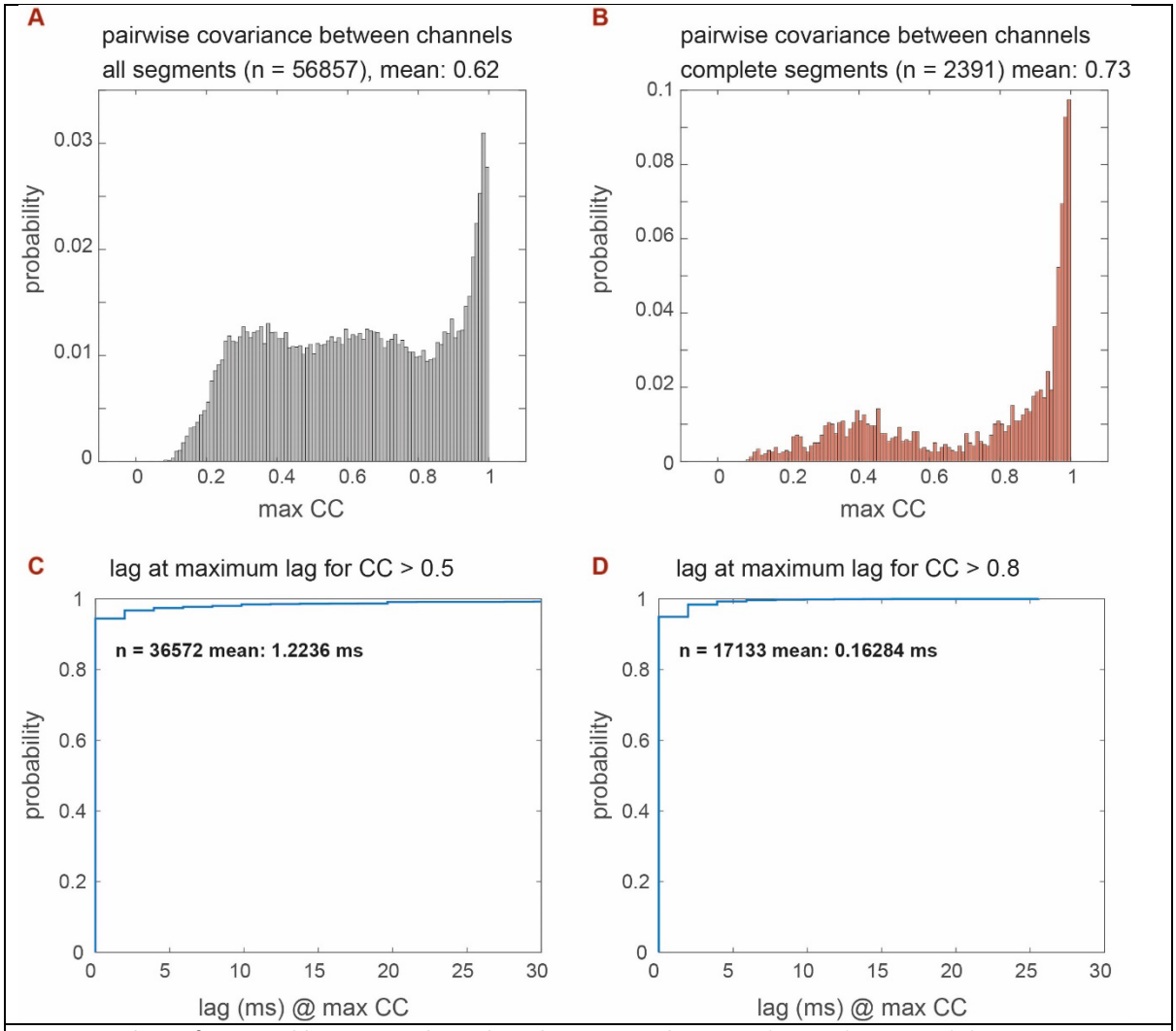

Fig. S9. Analysis of temporal lags across channels within an episode. For each episode, we used the cross-covariance (CC) function (*xcov* function in MATLAB) to find the best match (highest covariance) between the channel with the maximum energy (for that episode), and all other channels. **A.** Distribution of all CC obtained with this procedure. **B.** Distributions of CCs for *complete* episodes. **C.** Cumulative distribution of lags (in absolute values) that yield the highest CC. To exclude non-oscillating channels from this analysis, we only considered channels that had a CC of at least 0.5 (a low threshold considering the distribution shown in A). The rationale for setting a threshold on the CC is that non-oscillating channels will not yield high correlations with the highest-amplitude, reference oscillating channel **D.** Cumulative lag distributions when considering channels with CCs of at least 0.8. Mean values are indicated in panels C and D and are very small relative to a theta cycle. This analysis revealed that percentage of channels with lags smaller than 10 ms (in absolute value) are 85% across all channels in all episodes (no CC threshold), 98% for all channels with a CC > 0.5 (as in panel C), and 99.9% when considering channels with CC > 0.8 (panel D). A period of 10 ms represents 1/20 of a 5 Hz theta cycle and thus assigning the oscillation phase based on one channel is expected to induce a negligible jitter in our phase estimates.

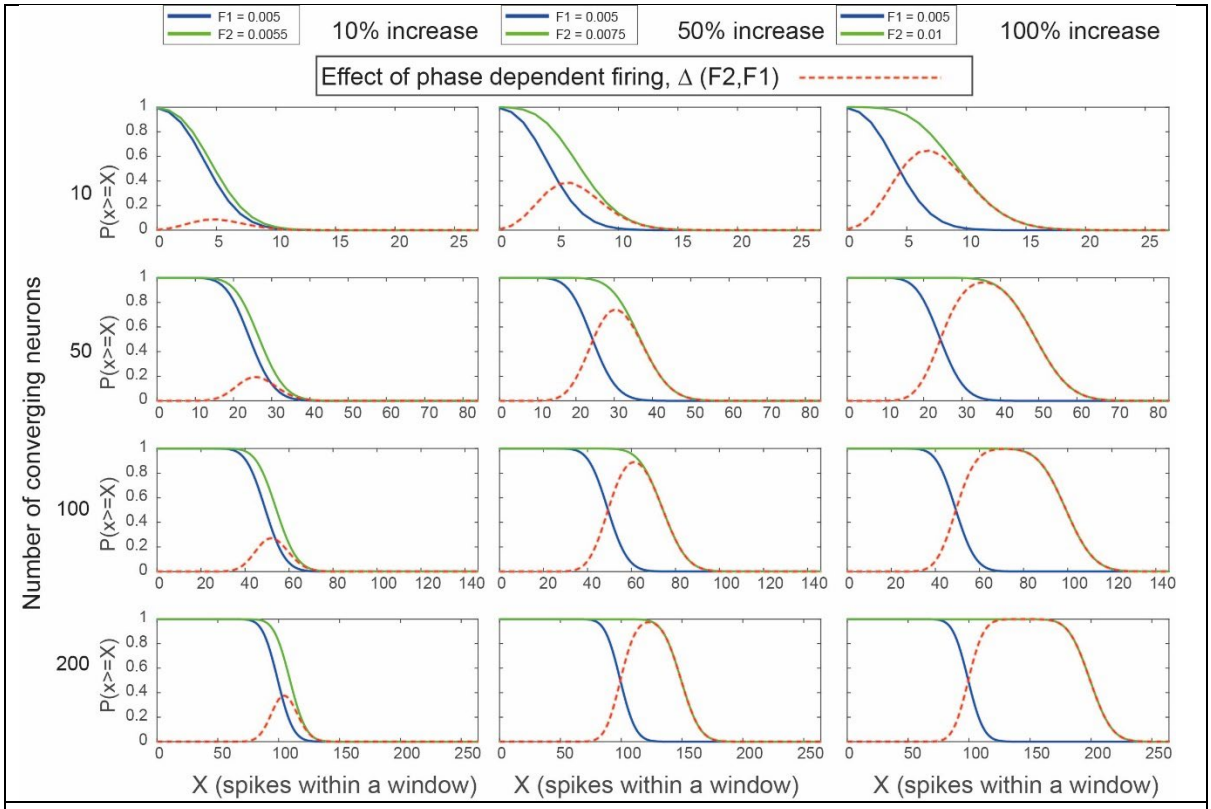

Fig. S10. Effects of phase dependent firing on the probability of coincident spikes. Each panel shows the probability to obtain a certain number of spikes (or more), within a single integration window of 100 ms (i.e., half a 5 Hz theta cycle). Each row represents a different number of neurons (from top to bottom: 10, 50, 100, 200) and each column represents a different degree of spike time locking, quantified by the firing rate within that period. In all of these examples, the baseline rate (without spike time locking) is 5Hz which corresponds to a probability of firing of 0.005 within a 1 ms window. In each column, the degree of locking is different, and increases from left to right, assuming rates that are 1.1x, 1.5x, or 2x the baseline rate. Note that a 1.5-fold increase implies that 60% of all spikes are generated within half a cycle while a 2-fold increase within half a cycle from a uniform distribution implies that 2/3 of the spikes are emitted within half a cycle. In all plots, blue traces indicate the probability under uniform firing, and green traces indicate the probability with phase dependent firing. Broken red traces represent the difference between the two cumulative probabilities. This analysis highlights the benefit of even modest spike phase locking. The difference between uniform and phase dependent distributions increases with the number of neurons and the degree of locking (and remains true across all realistic baseline firing rates). Note the different horizontal scaling between the different rows.

Acknowledgements

This work was supported by Deutsche Forschungsgemeinschaft (German Research Foundation) 378028035 to Y.B.S. and M.S and German-Israeli Foundation for Scientific Research and Development 1-1193-153.13/2012 to Y.B.S. and M.S. Israeli Science Foundation (ISF) grant (1703/16) for Y.B.S. A.K. was supported by Lady Davis postdoctoral fellowship, IL.

References

ACKELS, T., JORDAN, R., SCHAEFER, A. T. & FUKUNAGA, I. 2020. Respiration-Locking of Olfactory Receptor and Projection Neurons in the Mouse Olfactory Bulb and Its Modulation by Brain State. *Front Cell Neurosci,* 14**,** 220.

BANSAL, R., NAGEL, M., STOPKOVA, R., SOFER, Y., KIMCHI, T., STOPKA, P., SPEHR, M. & BEN-SHAUL, Y. 2021. Do all mice smell the same? Chemosensory cues from inbred and wild mouse strains elicit stereotypic sensory representations in the accessory olfactory bulb. *BMC Biology,* 19**,** 133.

BATHELLIER, B., LAGIER, S., FAURE, P. & LLEDO, P. M. 2006. Circuit properties generating gamma oscillations in a network model of the olfactory bulb. *J Neurophysiol,* 95**,** 2678-91.

BEN-SHAUL, Y., KATZ, L. C., MOONEY, R. & DULAC, C. 2010. In vivo vomeronasal stimulation reveals sensory encoding of conspecific and allospecific cues by the mouse accessory olfactory bulb. *Proc Natl Acad Sci U S A,* 107**,** 5172-7.

BEN SHAUL, Y., KATZ, L., MOONEY, R. & DULAC, C. 2010. In-vivo Vomeronasal Stimulation reveals Sensory Encoding of Conspecific and Allospecific Cues by the Mouse Accessory Olfactory Bulb. *PNAS,* in-press.

BERENS, P. 2009. CircStat: A MATLAB Toolbox for Circular Statistics. *Journal of Statistical Software,* 31**,** 1 - 21.

BERGAN, J. F., BEN-SHAUL, Y. & DULAC, C. 2014. Sex-specific processing of social cues in the medial amygdala. *Elife (Cambridge),* 3**,** e02743.
BINNS, K. E. & BRENNAN, P. A. 2005. Changes in electrophysiological activity in the accessory olfactory bulb and medial amygdala associated with mate recognition in mice. *Eur J Neurosci,* 21**,** 2529-37.
BUCK, L. B. 2004. Olfactory receptors and odor coding in mammals. *Nutr Rev,* 62**,** S184-8; discussion S224-41.
BURTON, S. D. & URBAN, N. N. 2021. Cell and circuit origins of fast network oscillations in the mammalian main olfactory bulb. *Elife,* 10.
BUZSÁKI, G. 2006. *Rhythms of the brain,* Oxford ; New York, Oxford University Press.
BUZSAKI, G., ANASTASSIOU, C. A. & KOCH, C. 2012. The origin of extracellular fields and currents--EEG, ECoG, LFP and spikes. *Nat Rev Neurosci,* 13**,** 407-20.
CADIZ-MORETTI, B., OTERO-GARCIA, M., MARTINEZ-GARCIA, F. & LANUZA, E. 2014. Afferent projections to the different medial amygdala subdivisions: a retrograde tracing study in the mouse. *Brain Struct Funct*.
CENIER, T., DAVID, F., LITAUDON, P., GARCIA, S., AMAT, C. & BUONVISO, N. 2009. Respiration-gated formation of gamma and beta neural assemblies in the mammalian olfactory bulb. *Eur J Neurosci,* 29**,** 921-30.
CHAPUT, M. A. 1986. Respiratory-phase-related coding of olfactory information in the olfactory bulb of awake freely-breathing rabbits. *Physiol Behav,* 36**,** 319-24.
CHONG, E. & RINBERG, D. 2018. Behavioral readout of spatio-temporal codes in olfaction. *Curr Opin Neurobiol,* 52**,** 18-24.
CICHY, A., ACKELS, T., TSITOURA, C., KAHAN, A., GRONLOH, N., SOCHTIG, M., ENGELHARDT, C. H., BEN-SHAUL, Y., MULLER, F., SPEHR, J.*, et al.* 2015. Extracellular pH regulates excitability of vomeronasal sensory neurons. *J Neurosci,* 35**,** 4025-39.
CLELAND, T. A. 2014. Construction of odor representations by olfactory bulb microcircuits. *Prog Brain Res,* 208**,** 177-203.
CSICSVARI, J., HENZE, D. A., JAMIESON, B., HARRIS, K. D., SIROTA, A., BARTHO, P., WISE, K. D. & BUZSAKI, G. 2003. Massively parallel recording of unit and local field potentials with silicon-based electrodes. *J Neurophysiol,* 90**,** 1314-23.
CURY, K. M. & UCHIDA, N. 2010. Robust odor coding via inhalation-coupled transient activity in the mammalian olfactory bulb. *Neuron,* 68**,** 570-85.
DALAL, T. & HADDAD, R. 2022. Upstream gamma-synchronization enhances odor processing in downstream neurons. *Cell Rep,* 39**,** 110693.
DAUBECHIES, I., LU, J. F. & WU, H. T. 2011. Synchrosqueezed wavelet transforms: An empirical mode decomposition-like tool. *Applied and Computational Harmonic Analysis,* 30**,** 243-261.
DAVID, F., COURTIOL, E., BUONVISO, N. & FOURCAUD-TROCME, N. 2015. Competing Mechanisms of Gamma and Beta Oscillations in the Olfactory Bulb Based on Multimodal Inhibition of Mitral Cells Over a Respiratory Cycle. *eNeuro,* 2.
DAVISON, I. G. & EHLERS, M. D. 2011. Neural circuit mechanisms for pattern detection and feature combination in olfactory cortex. *Neuron,* 70**,** 82-94.
DHAWALE, A. K., HAGIWARA, A., BHALLA, U. S., MURTHY, V. N. & ALBEANU, D. F. 2010. Non-redundant odor coding by sister mitral cells revealed by light addressable glomeruli in the mouse. *Nat Neurosci,* 13**,** 1404-12.
DULAC, C. & AXEL, R. 1995. A novel family of genes encoding putative pheromone receptors in mammals. *Cell,* 83**,** 195-206.
DULAC, C. & AXEL, R. 1998. Expression of candidate pheromone receptor genes in vomeronasal neurons. *Chem Senses,* 23**,** 467-75.
DULAC, C. & WAGNER, S. 2006. Genetic analysis of brain circuits underlying pheromone signaling. *Annu Rev Genet,* 40**,** 449-67.

EINEVOLL, G. T., KAYSER, C., LOGOTHETIS, N. K. & PANZERI, S. 2013. Modelling and analysis of local field potentials for studying the function of cortical circuits. *Nat Rev Neurosci,* 14**,** 770-85.
FAN, S. & LUO, M. 2009. The organization of feedback projections in a pathway important for processing pheromonal signals. *Neuroscience,* 161**,** 489-500.
FERRERO, D. M., MOELLER, L. M., OSAKADA, T., HORIO, N., LI, Q., ROY, D. S., CICHY, A., SPEHR, M., TOUHARA, K. & LIBERLES, S. D. 2013. A juvenile mouse pheromone inhibits sexual behaviour through the vomeronasal system. *Nature,* 502**,** 368-71.
FOURCAUD-TROCME, N., BRIFFAUD, V., THEVENET, M., BUONVISO, N. & AMAT, C. 2018. In vivo beta and gamma subthreshold oscillations in rat mitral cells: origin and gating by respiratory dynamics. *J Neurophysiol,* 119**,** 274-289.
FREDERICK, D. E., BROWN, A., BRIM, E., MEHTA, N., VUJOVIC, M. & KAY, L. M. 2016. Gamma and Beta Oscillations Define a Sequence of Neurocognitive Modes Present in Odor Processing. *J Neurosci,* 36**,** 7750-67.
FU, X., YAN, Y., XU, P. S., GEERLOF-VIDAVSKY, I., CHONG, W., GROSS, M. L. & HOLY, T. E. 2015. A Molecular Code for Identity in the Vomeronasal System. *Cell,* 163**,** 313-23.
FUKUNAGA, I., HERB, J. T., KOLLO, M., BOYDEN, E. S. & SCHAEFER, A. T. 2014. Independent control of gamma and theta activity by distinct interneuron networks in the olfactory bulb. *Nat Neurosci,* 17**,** 1208-16.
GAO, Y., BUDLONG, C., DURLACHER, E. & DAVISON, I. G. 2017. Neural mechanisms of social learning in the female mouse. *Elife,* 6.
GEORGE PAXINOS , K. B. J. F. 2001. *The Mouse Brain in Stereotaxic Coordinates,* San Diego, Academic press.
GILL, J. V., LERMAN, G. M., ZHAO, H., STETLER, B. J., RINBERG, D. & SHOHAM, S. 2020. Precise Holographic Manipulation of Olfactory Circuits Reveals Coding Features Determining Perceptual Detection. *Neuron*.
GORIN, M., TSITOURA, C., KAHAN, A., WATZNAUER, K., DROSE, D. R., ARTS, M., MATHAR, R., O'CONNOR, S., HANGANU-OPATZ, I. L., BEN-SHAUL, Y.*, et al.* 2016. Interdependent Conductances Drive Infraslow Intrinsic Rhythmogenesis in a Subset of Accessory Olfactory Bulb Projection Neurons. *J Neurosci,* 36**,** 3127-44.
GSCHWEND, O., BEROUD, J. & CARLETON, A. 2012. Encoding odorant identity by spiking packets of rate-invariant neurons in awake mice. *PLoS One,* 7**,** e30155.
HADDAD, R., LANJUIN, A., MADISEN, L., ZENG, H., MURTHY, V. N. & UCHIDA, N. 2013. Olfactory cortical neurons read out a relative time code in the olfactory bulb. *Nat Neurosci,* 16**,** 949-57.
HAMMEN, G. F., TURAGA, D., HOLY, T. E. & MEEKS, J. P. 2014. Functional organization of glomerular maps in the mouse accessory olfactory bulb. *Nat Neurosci,* 17**,** 953-61.
HAZAN, L., ZUGARO, M. & BUZSAKI, G. 2006. Klusters, NeuroScope, NDManager: a free software suite for neurophysiological data processing and visualization. *J Neurosci Methods,* 155**,** 207-16.
HENDRICKSON, R. C., KRAUTHAMER, S., ESSENBERG, J. M. & HOLY, T. E. 2008. Inhibition shapes sex selectivity in the mouse accessory olfactory bulb. *J Neurosci,* 28**,** 12523-34.
ISHII, K. K., OSAKADA, T., MORI, H., MIYASAKA, N., YOSHIHARA, Y., MIYAMICHI, K. & TOUHARA, K. 2017. A Labeled-Line Neural Circuit for Pheromone-Mediated Sexual Behaviors in Mice. *Neuron,* 95**,** 123-137 e8.
ISHII, K. K. & TOUHARA, K. 2019. Neural circuits regulating sexual behaviors via the olfactory system in mice. *Neurosci Res,* 140**,** 59-76.
JIA, C., CHEN, W. R. & SHEPHERD, G. M. 1999. Synaptic organization and neurotransmitters in the rat accessory olfactory bulb. *J Neurophysiol,* 81**,** 345-55.
JIANG, H., SCHUELE, S., ROSENOW, J., ZELANO, C., PARVIZI, J., TAO, J. X., WU, S. & GOTTFRIED, J. A. 2017. Theta Oscillations Rapidly Convey Odor-Specific Content in Human Piriform Cortex. *Neuron,* 94**,** 207-219 e4.

JOHN, S. R., DAGASH, W., MOHAPATRA, A. N., NETSER, S. & WAGNER, S. 2022. Distinct Dynamics of Theta and Gamma Rhythmicity during Social Interaction Suggest Differential Mode of Action in the Medial Amygdala of Sprague Dawley Rats and C57BL/6J Mice. *Neuroscience,* 493**,** 69-80.

JORDAN, R., FUKUNAGA, I., KOLLO, M. & SCHAEFER, A. T. 2018. Active Sampling State Dynamically Enhances Olfactory Bulb Odor Representation. *Neuron,* 98**,** 1214-1228 e5.

KAHAN, A. & BEN-SHAUL, Y. 2016. Extracting Behaviorally Relevant Traits from Natural Stimuli: Benefits of Combinatorial Representations at the Accessory Olfactory Bulb. *PLoS Comput Biol,* 12**,** e1004798.

KAUR, A. W., ACKELS, T., KUO, T. H., CICHY, A., DEY, S., HAYS, C., KATERI, M., LOGAN, D. W., MARTON, T. F., SPEHR, M.*, et al.* 2014. Murine pheromone proteins constitute a context-dependent combinatorial code governing multiple social behaviors. *Cell,* 157**,** 676-88.

KAY, L. M. 2014. Circuit oscillations in odor perception and memory. *Prog Brain Res,* 208**,** 223-51.

KAY, L. M. 2015. Olfactory system oscillations across phyla. *Curr Opin Neurobiol,* 31**,** 141-7.

KEPECS, A., UCHIDA, N. & MAINEN, Z. F. 2006. The sniff as a unit of olfactory processing. *Chem Senses,* 31**,** 167-79.

KEPECS, A., UCHIDA, N. & MAINEN, Z. F. 2007. Rapid and precise control of sniffing during olfactory discrimination in rats. *J Neurophysiol,* 98**,** 205-13.

KERSEN, D. E. C., TAVONI, G. & BALASUBRAMANIAN, V. 2022. Connectivity and dynamics in the olfactory bulb. *PLoS Comput Biol,* 18**,** e1009856.

KIMOTO, H., HAGA, S., SATO, K. & TOUHARA, K. 2005. Sex-specific peptides from exocrine glands stimulate mouse vomeronasal sensory neurons. *Nature,* 437**,** 898-901.

KOULAKOV, A., GELPERIN, A. & RINBERG, D. 2007. Olfactory coding with all-or-nothing glomeruli. *J Neurophysiol,* 98**,** 3134-42.

LANUZA, E., MARTINEZ-MARCOS, A., FONT, C. & MARTINEZ-GARCIA, F. 1996. Catecholaminergic interplexiform cells in the retina of lizards. *Vision Res,* 36**,** 1349-55.

LARRIVA-SAHD, J. 2008. The accessory olfactory bulb in the adult rat: a cytological study of its cell types, neuropil, neuronal modules, and interactions with the main olfactory system. *J Comp Neurol,* 510**,** 309-50.

LEFEVRE, L., COURTIOL, E., GARCIA, S., THEVENET, M., MESSAOUDI, B. & BUONVISO, N. 2016. Significance of sniffing pattern during the acquisition of an olfactory discrimination task. *Behav Brain Res,* 312**,** 341-54.

LESZKOWICZ, E., KHAN, S., NG, S., VED, N., SWALLOW, D. L. & BRENNAN, P. A. 2012. Noradrenaline-induced enhancement of oscillatory local field potentials in the mouse accessory olfactory bulb does not depend on disinhibition of mitral cells. *Eur J Neurosci,* 35**,** 1433-45.

LI, G. & CLELAND, T. A. 2017. A coupled-oscillator model of olfactory bulb gamma oscillations. *PLoS Comput Biol,* 13**,** e1005760.

LI, Q. & LIBERLES, S. D. 2015. Aversion and attraction through olfaction. *Curr Biol,* 25**,** R120-9.

LOSACCO, J., RAMIREZ-GORDILLO, D., GILMER, J. & RESTREPO, D. 2020. Learning improves decoding of odor identity with phase-referenced oscillations in the olfactory bulb. *Elife,* 9.

LUO, M., FEE, M. S. & KATZ, L. C. 2003. Encoding pheromonal signals in the accessory olfactory bulb of behaving mice. *Science,* 299**,** 1196-201.

MALNIC, B., HIRONO, J., SATO, T. & BUCK, L. B. 1999. Combinatorial receptor codes for odors. *Cell,* 96**,** 713-23.

MARKOPOULOS, F., ROKNI, D., GIRE, D. H. & MURTHY, V. N. 2012. Functional properties of cortical feedback projections to the olfactory bulb. *Neuron,* 76**,** 1175-88.

MEEKS, J. P., ARNSON, H. A. & HOLY, T. E. 2010. Representation and transformation of sensory information in the mouse accessory olfactory system. *Nat Neurosci,* 13**,** 723-30.

MEREDITH, M. 1994. Chronic recording of vomeronasal pump activation in awake behaving hamsters. *Physiol Behav,* 56**,** 345-54.

MEREDITH, M. & O'CONNELL, R. J. 1979. Efferent control of stimulus access to the hamster vomeronasal organ. *J Physiol,* 286**,** 301-16.
MITZDORF, U. 1985. Current source-density method and application in cat cerebral cortex: investigation of evoked potentials and EEG phenomena. *Physiol Rev,* 65**,** 37-100.
MOHRHARDT, J., NAGEL, M., FLECK, D., BEN-SHAUL, Y. & SPEHR, M. 2018. Signal detection and coding in the accessory olfactory system. *Chem Senses*.
OSAKADA, T., ISHII, K. K., MORI, H., EGUCHI, R., FERRERO, D. M., YOSHIHARA, Y., LIBERLES, S. D., MIYAMICHI, K. & TOUHARA, K. 2018. Sexual rejection via a vomeronasal receptor-triggered limbic circuit. *Nat Commun,* 9**,** 4463.
OSINSKI, B. L. & KAY, L. M. 2016. Granule cell excitability regulates gamma and beta oscillations in a model of the olfactory bulb dendrodendritic microcircuit. *J Neurophysiol,* 116**,** 522-39.
PARDO-BELLVER, C., MARTINEZ-BELLVER, S., MARTINEZ-GARCIA, F., LANUZA, E. & TERUEL-MARTI, V. 2017. Synchronized Activity in The Main and Accessory Olfactory Bulbs and Vomeronasal Amygdala Elicited by Chemical Signals in Freely Behaving Mice. *Sci Rep,* 7**,** 9924.
SCHOPPA, N. E. 2006. Synchronization of olfactory bulb mitral cells by precisely timed inhibitory inputs. *Neuron,* 49**,** 271-83.
SHPAK, G., ZYLBERTAL, A., YAROM, Y. & WAGNER, S. 2012. Calcium-activated sustained firing responses distinguish accessory from main olfactory bulb mitral cells. *J Neurosci,* 32**,** 6251-62.
SHUSTERMAN, R., SMEAR, M. C., KOULAKOV, A. A. & RINBERG, D. 2011. Precise olfactory responses tile the sniff cycle. *Nat Neurosci,* 14**,** 1039-44.
SMEAR, M., RESULAJ, A., ZHANG, J., BOZZA, T. & RINBERG, D. 2013. Multiple perceptible signals from a single olfactory glomerulus. *Nat Neurosci,* 16**,** 1687-91.
SMEAR, M., SHUSTERMAN, R., O'CONNOR, R., BOZZA, T. & RINBERG, D. 2011. Perception of sniff phase in mouse olfaction. *Nature,* 479**,** 397-400.
TAKAMI, S. & GRAZIADEI, P. P. 1991. Light microscopic Golgi study of mitral/tufted cells in the accessory olfactory bulb of the adult rat. *J Comp Neurol,* 311**,** 65-83.
TENDLER, A. & WAGNER, S. 2015. Different types of theta rhythmicity are induced by social and fearful stimuli in a network associated with social memory. *Elife,* 4.
THAKUR, G., BREVDO, E., FUCKAR, N. S. & WU, H. T. 2013. The Synchrosqueezing algorithm for time-varying spectral analysis: Robustness properties and new paleoclimate applications. *Signal Processing,* 93**,** 1079-1094.
TOLOKH, II, FU, X. & HOLY, T. E. 2013. Reliable sex and strain discrimination in the mouse vomeronasal organ and accessory olfactory bulb. *J Neurosci,* 33**,** 13903-13.
TSITOURA, C., MALINOWSKI, S. T., MOHRHARDT, J., DEGEN, R., DIBENEDICTIS, B. T., GAO, Y., WATZNAUER, K., GERHOLD, K., NAGEL, M., WEBER, M.*, et al.* 2020. Synchronous Infra-Slow Oscillations Organize Ensembles of Accessory Olfactory Bulb Projection Neurons into Distinct Microcircuits. *J Neurosci,* 40**,** 4203-4218.
UCHIDA, N., POO, C. & HADDAD, R. 2014. Coding and transformations in the olfactory system. *Annu Rev Neurosci,* 37**,** 363-85.
VERHAGEN, J. V., WESSON, D. W., NETOFF, T. I., WHITE, J. A. & WACHOWIAK, M. 2007. Sniffing controls an adaptive filter of sensory input to the olfactory bulb. *Nat Neurosci,* 10**,** 631-9.
WACHOWIAK, M. 2011. All in a sniff: olfaction as a model for active sensing. *Neuron,* 71**,** 962-73.
WAGNER, S., GRESSER, A. L., TORELLO, A. T. & DULAC, C. 2006. A multireceptor genetic approach uncovers an ordered integration of VNO sensory inputs in the accessory olfactory bulb. *Neuron,* 50**,** 697-709.
WILSON, C. D., SERRANO, G. O., KOULAKOV, A. A. & RINBERG, D. 2017. A primacy code for odor identity. *Nat Commun,* 8**,** 1477.
WYSOCKI, C. J., WELLINGTON, J. L. & BEAUCHAMP, G. K. 1980. Access of urinary nonvolatiles to the mammalian vomeronasal organ. *Science,* 207**,** 781-3.

YOLES-FRENKEL, M., COHEN, O., BANSAL, R., HORESH, N. & BEN-SHAUL, Y. 2017. In vivo stimulus presentation to the mouse vomeronasal system: Surgery, experiment, setup, and software. *J Neurosci Methods,* 285**,** 19-32.

YOLES-FRENKEL, M., KAHAN, A. & BEN-SHAUL, Y. 2018. Temporal Response Properties of Accessory Olfactory Bulb Neurons: Limitations and Opportunities for Decoding. *J Neurosci,* 38**,** 4957-4976.

ZELANO, C., JIANG, H., ZHOU, G., ARORA, N., SCHUELE, S., ROSENOW, J. & GOTTFRIED, J. A. 2016. Nasal Respiration Entrains Human Limbic Oscillations and Modulates Cognitive Function. *J Neurosci,* 36**,** 12448-12467.

ZIBMAN, S., SHPAK, G. & WAGNER, S. 2011. Distinct intrinsic membrane properties determine differential information processing between main and accessory olfactory bulb mitral cells. *Neuroscience,* 189**,** 51-67.

ZYLBERTAL, A., KAHAN, A., BEN-SHAUL, Y., YAROM, Y. & WAGNER, S. 2015. Prolonged Intracellular Na+ Dynamics Govern Electrical Activity in Accessory Olfactory Bulb Mitral Cells. *PLoS Biol,* 13**,** e1002319.

ZYLBERTAL, A., YAROM, Y. & WAGNER, S. 2017a. The Slow Dynamics of Intracellular Sodium Concentration Increase the Time Window of Neuronal Integration: A Simulation Study. *Front Comput Neurosci,* 11**,** 85.

ZYLBERTAL, A., YAROM, Y. & WAGNER, S. 2017b. Synchronous Infra-Slow Bursting in the Mouse Accessory Olfactory Bulb Emerge from Interplay between Intrinsic Neuronal Dynamics and Network Connectivity. *J Neurosci,* 37**,** 2656-2672.